APPLICATION OF TIME SERIES SATELLITE DATA TO EARTH SCIENCE PROBLEMS

A Thesis

Presented in Partial Fulfillment of the Requirements for

the Degree Master of Science in the

Graduate School of The Ohio State University

By

Kee-Tae Kim, B.S.

* * * * *

The Ohio State University
1999

Master's Examination Committee:

Dr. Rongxing Li, Adviser

Dr. Kenneth C. Jezek

Dr. Alan J. Saalfeld

Approved by:

____

Adviser
Graduate Program in Geodetic Science
and Surveying

ABSTRACT

This paper is a demonstration of the usefulness of declassified historical satellite imagery for glaciological studies of ice shelf motion and ice sheet margin changes in the Antarctic Ice Sheet and explains how historic high-resolution satellite imagery can be used to study patterns of urban development and growth.

A sophisticated photogrammetric and mapping technique was employed to derive accurate positional information from the digitized image. The accurately orthorectified images were imported into a Geographic Information System (GIS) and compiled to other time series data to assess environmental changes of Earth's surface.

Comparison of ice sheet margin changes between 1963 and 1997 illustrates that the seaward margin of ice sheet advances and retreats in a complex fashion. The absence of a uniform trend in ice margin advance/retreat with latitude suggests that the ice margin position is controlled by local rather than global processes. The favorable comparison between the 1963 velocities and the 1997 instantaneous velocities suggests that large calving event did not effect Filchner Ice Shelf dynamics.

Declassified historical high-resolution satellite data were found to be suitable for establishing a benchmark for land use patterns in and around Columbus, Ohio for 1965. Comparison of these data with later land use maps shows that the urban area in and around Columbus approximately doubled since 1965.

Dedicated to my parents

ACKNOWLEDGMENTS

I would like to express my sincere thanks to: Dr. Rongxing Li and Dr. Kenneth C. Jezek for their help and support during this project; Dr. Alan J. Saalfeld for his participation as a committee member; and my colleagues in the Remote Sensing Lab at the Byrd Polar Research Center for their friendship and constant help.

I would also like to express my deepest thanks to my wife for her patience and support, my parents and in-laws for their willingness to help out, and to a good friend, Sungwoong, for his encouragement.

This research was supported by NASA Center of Excellence Grant and NASA Polar Ocean and Ice Sheets Program.

VITA

July, 1964	Born – Seoul, Korea
1993	B.S. Civil Engineering, Dankook University
1996	M.S. Civil Engineering, Yonsei University
1998 – present	Graduate Research Associate Remote Sensing Lab Byrd Polar Research Center The Ohio State University

FIELD OF STUDY

Major Field: Graduate Program in Geodetic Science and Surveying

TABLE OF CONTENTS

LIST OF TABLES

LIST OF FIGURES

CHAPTER 1

INTRODUCTION

1.1 Early Satellite Photo Reconnaissance

A few short years after the launch of the Russian Sputnik in October 1957, high-resolution spaceborne camera systems gathered photo reconnaissance imagery of the Earth's surface. CORONA, ARGON, and LANYARD were the first three operational imaging satellite reconnaissance systems [McDonald, 1995]. These satellites operated between August 1960 and May 1972 and were developed in response to the uncertainties and anxieties created by the Cold War. Observations were made in utmost secrecy so that targeted nations would not be alerted to the overhead photography [McDonald, 1995].

These early reconnaissance satellites carried a single panoramic camera, a single frame camera, or two panoramic cameras. Resolution of the imagery ranged from 140 to 2 meters. Land coverage for the individual panoramic camera images was approximately 200 kilometers by 16 kilometers. Single frame camera coverage was 540 kilometers by 540 kilometers.

On February 22, 1995, the President of the United States ordered declassification of this historic satellite imagery for use in environmental science. The order caused the declassification of more than 800,000 images of the Earth's surface. For the first time, those 1960 vintage images became available to the general scientific community.

The reconnaissance satellite data are important because they extend the record of spaceborne observations back in time by a full decade. Prior to their release, environmental researchers were limited to airborne data as a source for high-resolution broad-scale coverage before 1972, which was the year the first LANDSAT mission was launched. With these historic satellite records now available, researchers potentially can explore the evolution of a host of scientific processes and potentially provide more precise information related to Earth science problems such as natural resources, land management, and bio-diversity monitoring [McDonald, 1995].

1.2 Why Satellites

Satellite imagery is particularly valuable because of accessibility to any part of the world, large spatial coverage for placing changes in a regional context, and increasing resolution for better interpretation. LANDSAT carried the multi-spectral scanner (MSS) which viewed the earth in 5 spectral bands from the optical to infrared at resolutions from 80m to 240m. Similar instruments followed MSS with current data from the SPOT satellite available at 10m resolution (panchromatic) over frames 60 km x 60 km in size. Table 1.1 shows a summary of relevant earth observation satellites and their capabilities.

Sensor System	Swath	Spectral Range	Spatial Resolution	Operations
NOAA AVHRR	2700 km	0.58 – 12.5 μm	1100 m	1978 – Present
LANDSAT MSS	185 km	0.50 – 12.6 μm	80 – 240 m	1972 – 1992
LANDSAT (E)TM	185 km	0.45 – 12.5 μm	30 – 120 m	1982 – Present
LANDSAT ETM+	185 km	0.45 – 12.5 μm	15 – 120 m	1999 – present
SPOT Multspectral	60 km	0.50 – 0.89 μm	20 m	1986 – Present
SPOT Panchromatic	60 km	0.51 – 0.73 μm	10 m	1986 – Present
ERS-1 & 2	100 km	5.3 GHz C-band	30 m	1991 – Present
RADARSAT	100 km	5.3 GHz C-band	25 m	1995 – Present

Table 1.1: Relevant Terrestrial Satellites

1.3 Applications of Early Photo Reconnaissance Satellite Data

Shortly after the release of Declassified Intelligence Satellite Photography (DISP), several researchers began using the historic high-resolution satellite data. Most work focused on the two polar ice sheet of Antarctica and Greenland. Jezek (1998) examined how different Antarctic flow regimes have changed over the 35-year interval between CORONA and RADARSAT. Optical CORONA imagery from 1963, optical SPOT imagery from 1995, and microwave RADARSAT imagery from 1997 were used as a data set. The examination showed that the rapid changes in ice sheet behavior are due to changes in the internal dynamics of the ice sheet. Similarly Bindschadler and Vornberger (1998) compared declassified satellite photography taken in 1963 with more recent satellite imagery to detect changes in the west Antarctic Ice Sheet since 1963. A mosaic of two images from the Advanced Very High Resolution Radiometer (AVHRR) collected in 1980 and 1992 and a series of panchromatic STOP images collected between 1989 and 1992 were used to compile a database of changes in the crevassing around Crary Ice Rise. The changes implied that the velocity field around Crary Ice Rise shifted during this century, and this shift in flow would increase the amount of ice passing north and east of Crary Ice Rise. Sohn and others (1998) detected changes in the Greenland ice sheet margins from 1962 to 1992 using a sequence of airborne and CORONA data. They showed that a climate warming might lead to a prolonged season of high calving rates, which would increase the annual calving flux of tidewater glaciers around Greenland. Bindschadler and Seider (1998) studied the collection of declassified intelligence satellite photography without significant cloud cover to outline the coastline of the Antarctic ice sheet. The US Geological Survey plans to produce coastal-change and glaciological maps of the Antarctica Peninsula over as much as 32 years where ARGON and European Space Agency Remote Sensing Satellite radar images exist [Williams and Ferrigno, 1998].

1.4 Objectives and Study Areas

The objective of this research is to explore how sophisticated geodetic and mapping techniques can be applied to the declassified data and to determine what new scientific applications can result from a more rigorous analysis. This research introduces differential rectification, which is the most accurate rectification technique, to rigorously geocode, mosaic, and create geometrically accurate orthorectified imagery using the DISP data. With those techniques, this research develops analysis procedures to study how environmental conditions have changed in one of the most remote parts of the world, Antarctica. The techniques are also applied to imagery collected over the urban setting of Columbus Ohio to test the robustness of the approach for studying a diversity of terrain and environments.

The study is divided into two applications: glaciological mapping of the east Antarctic Ice Sheet and mapping urban development in the metropolitan area of Columbus Ohio. Chapter II summarizes the data types, characteristics, and extents of DISP, RADARSAT-1, LANDSAT, and Landuse/Landcover (LULC) data. Chapter III covers the processes of geometrically correcting an image so that it can be represented on a planar surface, conforms to other images, and has the integrity of a map. Chapter IV and V illustrate applications of the data.

CHAPTER 2

DATA DESCRIPTIONS

1963 (Antarctica) and 1965 (Columbus) declassified satellite records, 1997 RADARSAT, 1994 LANDSAT, and 1976 USGS Landuse/Landcover vector data were used to compile two databases for investigating environmental changes in both rural and natural environments. This chapter summarizes the data types, characteristics and extents.

2.1 Declassified Intelligence Satellite Photography (DISP)

Declassified intelligence satellite photographs (DISP) were collected during a series of missions between 1960 and 1972. The intelligence community used the designators KH-1, KH-2, KH-3, KH-4, KH-4A and KH-4B for the CORONA systems. ARGON systems were designated KH-5 and the LANYARD systems KH-6. Early systems (KH-1, KH-2, KH-3, and KH-6) carried a single panoramic camera, or a single frame camera (KH-5), while the later systems (KH-4, KH-4A and KH-4B) carried two panoramic cameras with

30 degrees separation angle. Table 2.1 shows the spatial and temporal characteristics of the declassified intelligence satellite imagery.

The image data were recorded on high-resolution photographic, black and white as well as color, positive transparency film. The best resolution of the imagery is 2 meters, and the lowest resolution is approximately 140 meters. Land coverage for the individual panoramic camera images was approximately 200 kilometers by 16 kilometers. Single frame camera coverage was 540 kilometers by 540 kilometers.

System	KH-4A	KH-4B	KH-5
Camera Type	Panoramic	Panoramic	Frame
Film Format (mm)	70 x 760	70 x 760	120 x 120
Focal Length (mm)	610	610	76
Resolution of Film (lp/mm)	120	160	30
Ground Resolution(m)	3	2	138
Nominal Altitude (km)	180	145.8	313.2
Ground Coverage(km)	19 x 259	15 x 210	540 x 540
Period of Operation	1963 – 1969	1967 – 1972	1961 – 1964
Photo Scale on Film	1:305,000	1:247,500	1:4,250,000

Table 2.1: Characteristics of CORONA and ARGON [McDonald, 1995]

Figure 2.1 reproduces examples of ARGON and CORONA data. Both figure are browse images with 72-dpi resolution. They were downloaded from the web-based

Global Land Information System (GLIS) of the USGS Eros Data Center. Figure 2.1 (a) shows the Filchner Ice Shelf of east Antarctica captured by the ARGON frame camera on November 3, 1963. Figure 2.1 (b) shows a part of Columbus Ohio captured by the CORONA panoramic camera on October 29, 1965. Figure 2.2 (a) shows ARGON map coverage used for study of east Antarctica. Figure 2.2 (b) shows CORONA map coverage used for study of the metropolitan area of Columbus Ohio.

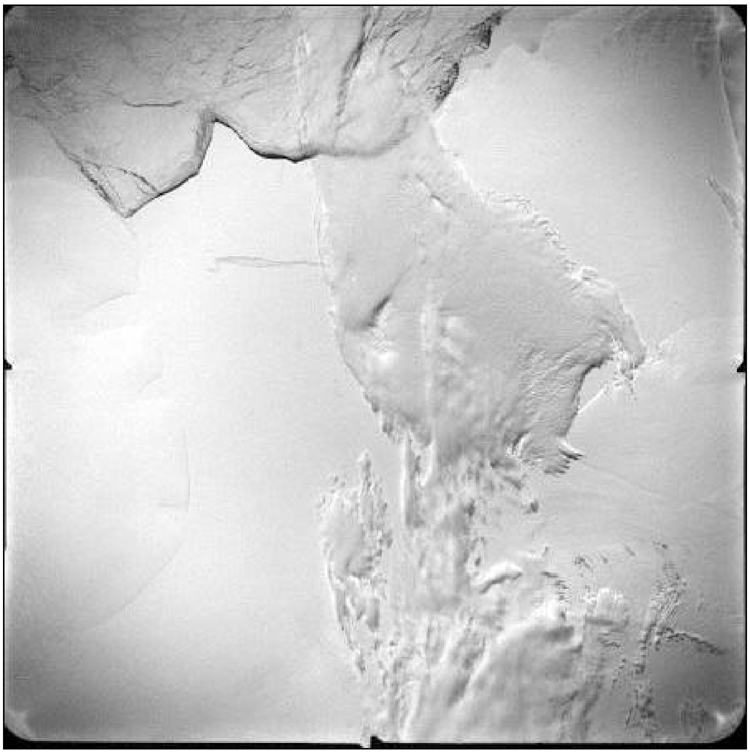

Figure 2.1 (a): An example of full ARGON photographic transparency of the Filchner Ice Shelf in Antarctica (540 km x 540 km). The actual size of the data product is 120 x 120mm.

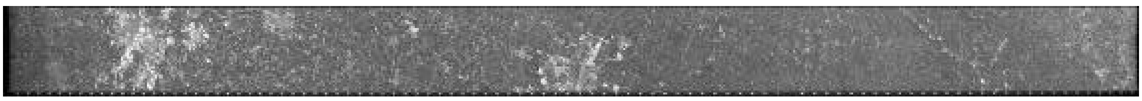

Figure 2.1 (b): An example of full CORONA photographic transparency of a part of Columbus Ohio (19 km x 259 km). The actual size of data product is 70 x 760mm.

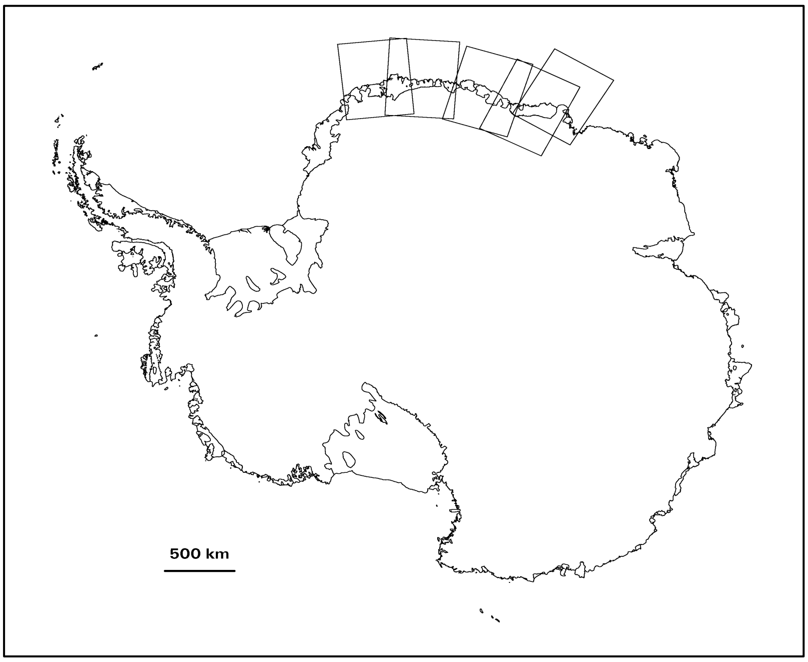

Figure 2.2 (a): ARGON coverage of the east Antarctic ice sheet

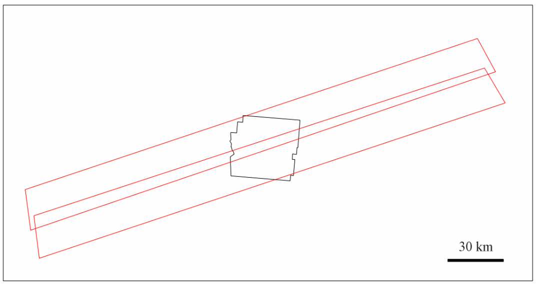

Figure 2.2 (b): CORONA coverage of Franklin County, Ohio

2.2 RADARSAT Data and DEM for Glaciological Mapping

Between September 19 and October 14, 1997, the Canadian RADARSAT-1 was used to successfully acquire the first, high-resolution, synthetic aperture radar (SAR) image data set of the entire Antarctic Continent. RADARSAT carried a C-band SAR capable of viewing the Earth surface with resolutions better than 25 meters. Ground coverage of each RADARSAT image data is 100 kilometer by 100 kilometers. The RADARSAT Antarctic Mapping Project (RAMP) produced a complete, seamless, high-resolution digital SAR mosaic of Antarctica [Jezek *et. al.*, 1999]. A portion of the mosaic is shown in Figure 2.3. This is one of the study areas for this paper.

A high-resolution digital elevation model (DEM) of the Antarctic used for terrain correcting the RADARSAT SAR imagery was applied to the ARGON imagery to eliminate the effect of relief displacements on the photographs taken over varied terrain. For the steeper ice sheet perimeter of Antarctica, it has a horizontal resolution of 200 meters and a vertical accuracy of 35 meters [Liu and others, 1999]. The hill shaded DEM of the study area is shown in Figure 2.4.

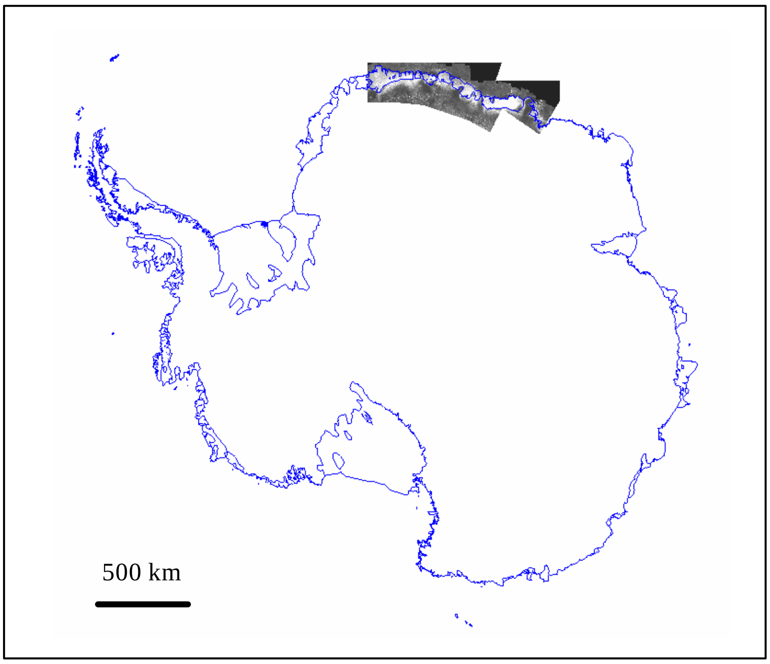

Figure 2.3: A portion of RADARSAT SAR mosaic over the east Antarctic ice sheet

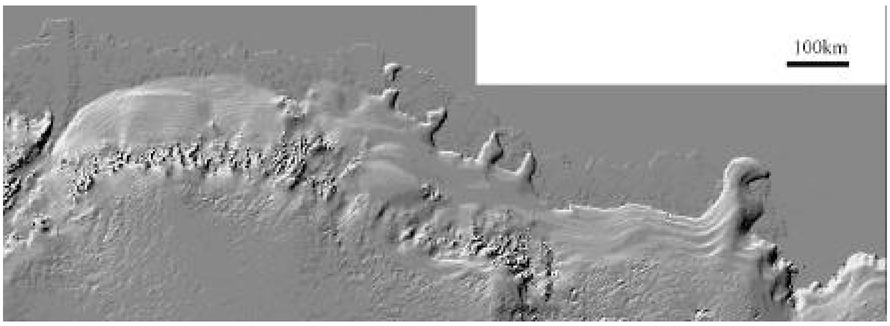

Figure 2.4: Hill Shaded DEM of the east Antarctic ice sheet

2.3 LANDSAT and Landuse/Landcover (LULC) data for Urban Mapping

Early reconnaissance satellite data, more recent land-use coverage maps, and more recent satellite images were combined to monitor changes of the metropolitan area of Columbus, Ohio over the last 30 years. The land-use maps for this study are the US Geological Survey LULC data. A Landsat TM image acquired in 1994 is also used. The use of these time series data allowed us to illustrate land-use changes that have occurred over time as a result of urbanization.

The 1994 Landsat TM image (Figure 2.5) over the metropolitan area of Columbus Ohio is a composite of bands 1, 2, 3, and 4. The image pixel size is 25 meters, which represents a slight over sampling of the nominal 30-m Landsat TM pixel. 1:250,000 scale LULC digital data (Figure 2.6) were collected by the US Geological Survey between the mid 1970s and early 1980s. The LULC data define urban or built-up land classes by seven sub-categories: residential, commercial and services, industrial, transportation, industrial and commercial complexes, mixed urban or built-up land, and other urban or built-up land.

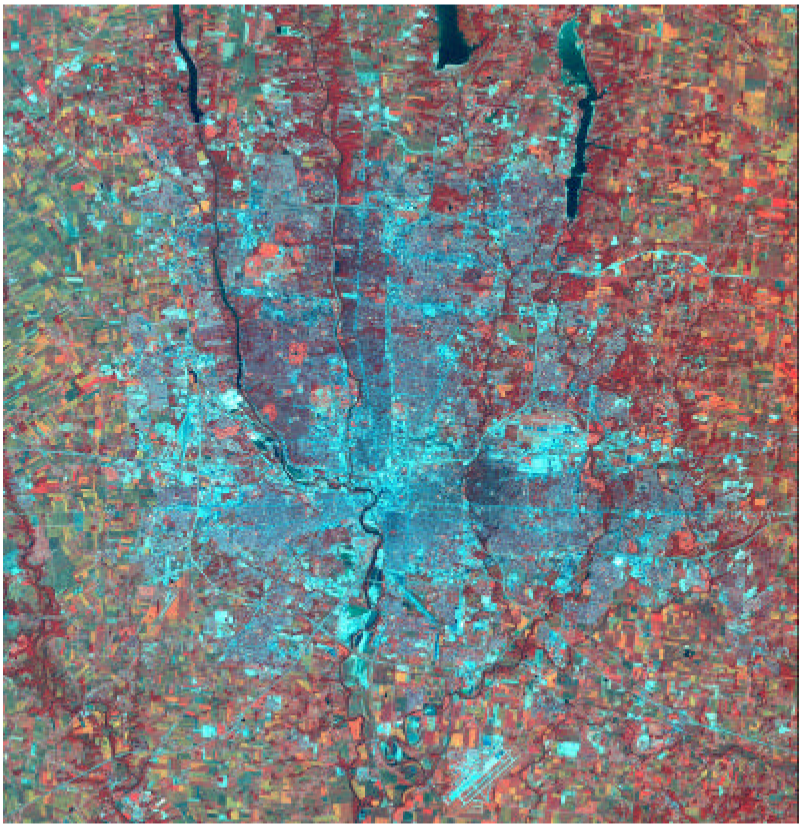

Figure 2.5: LANDSAT image (a composite of bands 1, 2, 3 and 4) of

Franklin County, Ohio [from Ohio Department of Natural Resources]

(A false-color composite of bands: band1-blue, band2- green, and band4-red)

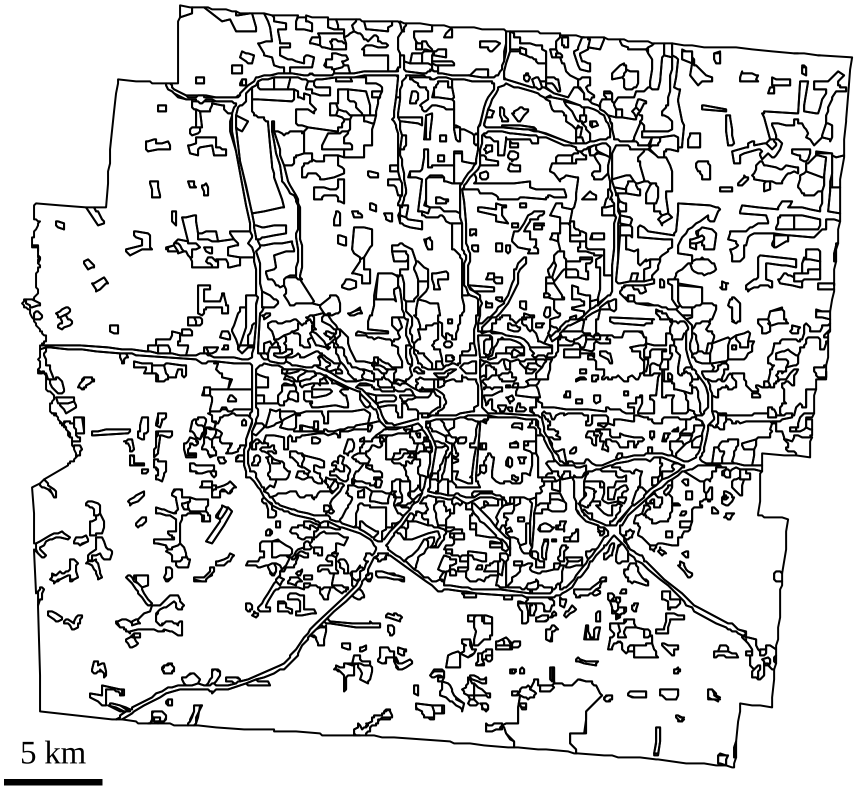

Level I (polygons)	Level II	
	LULC code	Landuse type
Urban or Built-up Land	11	Residential
	12	Commercial and Services
	13	Industrial
	14	Transportation, Communications, and Utilities
	15	Industrial and Commercial Complexes
	16	Mixed Urban or Built-up Land
	17	Other Urban or Built-up Land

Figure 2.6: 1:250,000-scale USGS LULC map of Franklin County, Ohio.

CHAPTER 3

IMAGE PROCESSING OF DISP

Raw, remotely sensed image data gathered by a satellite are representations of the irregular surface of the Earth. Because they do not have a uniform scale, we cannot simply measure distances on a satellite image. Instead, digital rectification techniques must be used to generate a uniform-scale, image-map. Two different types of digital rectification techniques were used to correct the geometric distortions of DISP photography. Differential rectification using a DEM was applied to the Antarctic area with varied terrain surface. First order polynomial rectification was applied to the metropolitan area of Columbus Ohio with relatively small, flat terrain surface. This chapter covers the processes of geometrically and radiometrically correcting DISP imagery so that it can be represented on a planar surface, conform to other images, and have the integrity of a map.

3.1 Scanning for Mapping Applications of DISP

The ARGON photography has a film resolution of 30 line-pair/mm, and the CORONA 120 line-pair/mm (Table 2.1). Each dimension of one resolution element is as follows:

$$\frac{1mm}{30\,lp} \times \frac{1000mm}{mm} = 33\,mm/lp$$

$$\frac{1mm}{120\,lp} \times \frac{1000mm}{mm} = 8.33\,mm/lp$$

Sampling theory is used to determine the range of acceptable spot sizes that will preserve the DISP photo resolution [Light, 1993]:

$$\frac{33mm}{2\sqrt{2}} \le scan\ spot\ size \le \frac{33mm}{2} \Rightarrow 11mm \le scan\ spot\ size \le 17mm$$

$$\frac{8.33mm}{2\sqrt{2}} \le scan\ spot\ size \le \frac{8.33mm}{2} \Rightarrow 2mn \le scan\ spot\ size \le 4mm$$

DISP photographs were scanned at 7-µm resolution using the INTERGRAPH PhotoScan TD® Scanner. The scanner is high-resolution radiometrically and geometrically precise flatbed scanning sys tem.

3.2 Differential Rectification of ARGON Photography

3.2.1 Image Refinements

Raw digital images collected from the photo reconnaissance satellite usually have such significant geometric distortions that they cannot be used as maps, compared with maps or compared to each other. These distortions stem from sources such as camera lens distortion, atmospheric refraction and Earth curvature. To begin the mapping process, we have to correct for all systematic distortions affecting the image coordinates.

For measurements made on ARGON photography, the photographs are only corrected for Earth's curvature, which far overweighs errors, introduced by the other distortions. For example, radial displacement due to the effect of atmospheric refraction was smaller than 1.2-μm because of the extremely small ratio of flying height to focal length. The measuring accuracy (1-2 pixels) using ARGON photography also outweighs displacements due to camera lens distortion and atmospheric refraction. However, the effect of Earth curvature caused the corner point on the photograph to be displaced about 2.2-mm (9-km in ground coordinates) inward from its actual position. These values were calculated at the photo corner where the highest elevation is 2 km in the study areas of east Antarctic. Figure 3.1 shows how serious the effect of Earth's curvature was made on the ARGON imagery. It can be computed as follow:

$$\Delta r = \frac{r^3 H}{2Rf^2}$$

where, Δr is inward radial displacement on the film, r radial distance, H flying height, R radius of Earth, and f focal length.

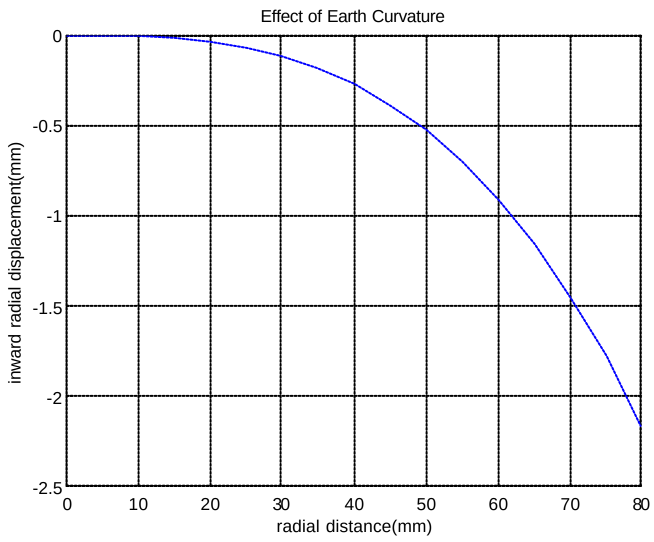

Figure 3.1: Effect of Earth curvature on ARGON photography.

3.2.2 Differential Rectification

Differential rectification corrects for terrain displacement and can be used if a digital elevation model (DEM) of the study area exists. A high-resolution DEM of the Antarctic has been constructed as part of the Radarsat Antarctic Mapping Project (RAMP) in 1999. The DEM used for terrain correcting 1997 RADARSAT SAR imagery was applied to the ARGON imagery to eliminate effect of the relief displacement on the photographs taken over varied terrain. Figure 3.2 shows relief displacements made by surface topography, which cause the top of a vertical feature to lie farther from the photo center than its base when a photograph is taken over terrain of varied relief. It can be computed as follow:

$$\Delta r = \frac{rh}{H}$$

where, Δr is outward radial displacement on the film, r radial distance, h topograhy, and H flying height.

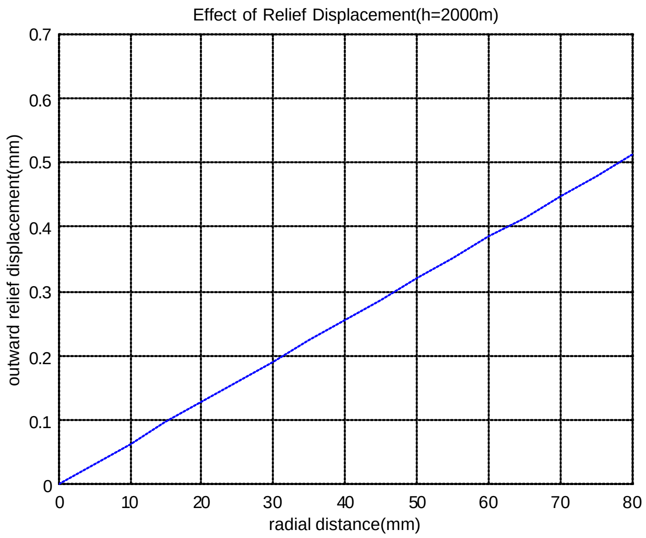

Figure 3.2: Effect of terrain relief displacement on ARGON photography.

Initial input to the differential rectification process consisted of three assumed camera calibration parameters and eleven ground control points (GCPs). Six exterior orientation parameters (EOPs) in the ground coordinates, three rotations and three positions, were determined by the space resection equation [Wolf, 1974]. As implemented in the commercial software package IMAGINE, differential rectification was performed as follows (Figure 3.3(a)), where (xo, yo) and (xi, yi) are the points in output coordinates (map) and input coordinates (image) respectively.

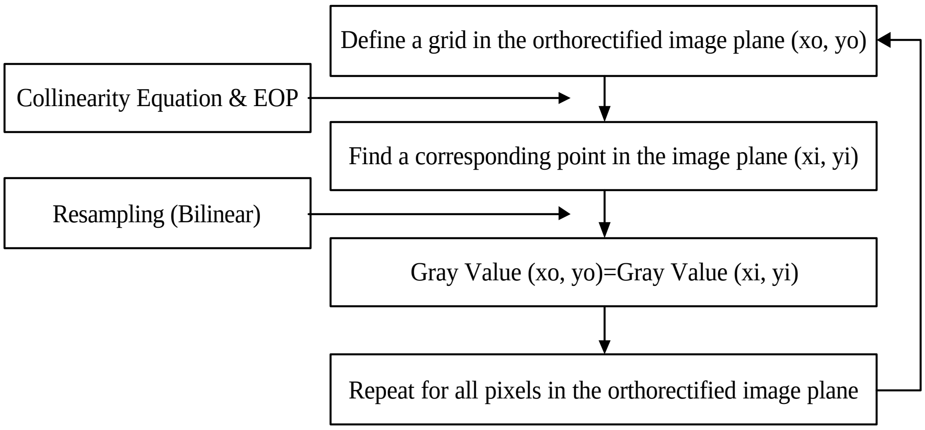

Figure 3.3 (a): Procedure of differential rectification

Once a regular grid over the orthorectified image plane was defined, we use the corresponding elevation and EOPs to compute the image coordinates (Figure 3.3(b)). The collinearity equations compute the location of the corresponding point in the original image. At this point, the position is typically non-integer, so that a gray value of the position was interpolated using a bilinear interpolation that uses four surrounding pixels to compute the gray value at the non-integer location. This is the most accurate rectification technique in that we can model the distortion parameters in the extended collinearity equations [Habib, 1999].

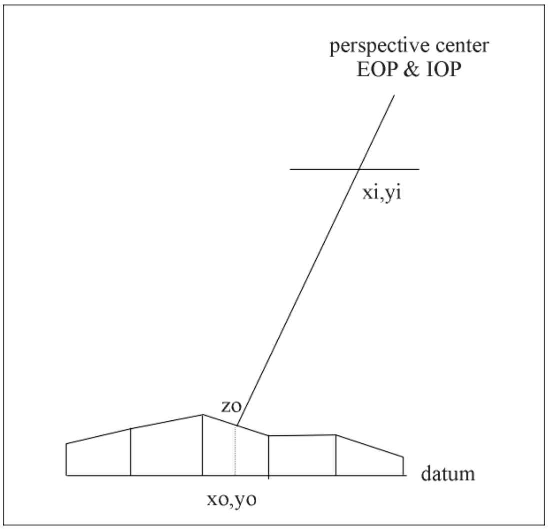

Figure 3.3 (b): Procedure of differential rectification

In this case, the accuracy of EOPs, GCPs, and DEM mainly affects the geometric quality of the orthorectified output image. The resolution of input imagery is another source that influences geometric fidelity of an output image, so that an enlargement factor is used to make better measurements of the GCPs. The enlargement of photography depends on the quality of the photography and the capability of the human operator to visualize the enlargement [Light, 1993]. The allowable enlargement factor for ARGON photography is as follow:

$$\frac{30\, lp/mm}{6\, lp/mm} \sim \frac{30\, lp/mm}{10\, lp/mm} = 5 \sim 3$$

Consequently, the ARGON photoraphy can be enlarged to pixel sizes of about 33μm/ 3 = 10-μm.

3.3.3 Least Square Adjustment

The mathematical model that relates the image coordinate to the ground coordinates is the collinearity equations:

$$\begin{aligned} x_{img} &= x_p - f \frac{r_{11}(X_{ground} - X_o) + r_{12}(Y_{ground} - Y_o) + r_{13}(Z_{ground} - Z_o)}{r_{31}(X_{ground} - X_o) + r_{32}(Y_{ground} - Y_o) + r_{33}(Z_{ground} - Z_o)} \\ y_{img} &= y_p - f \frac{r_{21}(X_{ground} - X_o) + r_{22}(Y_{ground} - Y_o) + r_{23}(Z_{ground} - Z_o)}{r_{31}(X_{ground} - X_o) + r_{32}(Y_{ground} - Y_o) + r_{33}(Z_{ground} - Z_o)} \end{aligned} \tag{3.1}$$

where

$x_{img},\ y_{img}$	are the observed image coordinates
$x_p,\ y_p,\ f$	are the assumed principal point coordinates and the known camera focal length;

$X_{ground}, Y_{ground}, Z_{ground}$ are the corresponding GCP coordinates;

X_o, Y_o, Z_o are camera station coordinates in ground system; and

$r_{11}, r_{12}, \cdots, r_{33}$ are rotation matrix elements as the functions of w, f, and k.

In this collinearity equation, image coordinates and GCP coordinates are the observations and the EOP coordinates are unknowns that we solve for. Let us start by introducing Gauss Markov model as follow:

$$y = Ax + e \qquad e \sim N(0, s_o^2 p^{-1}) \tag{3.2}$$

where

y is an (n x 1) vector of observations;

A is a matrix of partial derivatives relating the unknown parameters and the observations;

x is an (m x 1) normally distributed random vector of unknowns;

e is an (n x 1) vector of noise;

n is the number of observations;

m is the number of unknowns;

s_o^2 is the variance component or variance of observation of unit weight; and

p is an (n x n) weight matrix.

It must be noted that we consider the over-determined case only in photogrammetric approach. In other words, the number of observations is larger than the number of unknowns. In the least square adjustment, we set up a target function, which is to minimize the risk of choosing the wrong estimates. The target function is given by:

$$f(x) = e^T pe = \min(x) \tag{3.3}$$

$$f(x) = (y - Ax)^T p(y - Ax) = \min(x) \tag{3.4}$$

That is, we are looking for the estimates of unknowns that gives the minimum discrepancies between the observations. Taking the partial derivatives on the unknowns and usging Euler Lagrange necessary conditions, we can derive the equation for the least-square estimates.

$$\frac{\partial f}{\partial x} = 2A^T p(y - A\hat{x}) = 0 \tag{3.5}$$

$$A^T py = A^T pA\hat{x} \tag{3.6}$$

Assuming that $(A^T pA)$ is full rank matrix, that is, rk$(A^T pA)$ is m, the estimates for the unknown parameters can be expressed as follows:

$$\hat{x} = (A^T pA)^{-1} A^T py \tag{3.7}$$

Now, the dispersion of the estimated parameters $\hat{x}$ can be derived from the law of error propagation as follows:

$$
\begin{aligned}
D\{\hat{x}\} &= D\{(A^T pA)^{-1} A^T py\} \\
&= (A^T pA)^{-1} A^T pD\{y\} pA(A^T pA)^{-1} \\
&= (A^T pA)^{-1} A^T p\sigma_o{}^2 p^{-1} pA(A^T pA)^{-1} \\
&= \sigma_o{}^2 (A^T pA)^{-1} (A^T pA)(A^T pA)^{-1} \\
&= \sigma_o{}^2 (A^T pA)^{-1}
\end{aligned}
\tag{3.8}
$$

The predicted residual vector, $\tilde{e}$ can be computed as $\tilde{e} = y - A\hat{x}$. Finally the estimate for the variance component $\hat{\sigma}_o{}^2$ can be:

$$
\hat{\sigma}_o{}^2 = \frac{\tilde{e}^T p\tilde{e}}{n - m} \tag{3.9}
$$

where $(n - m)$ is the redundancy of the system. This means that the estimated variance covariance matrix of $\hat{x}$ is as follows:

$$
\hat{D}\{\hat{x}\} = \hat{\sigma}_o{}^2 (A^T pA)^{-1} \tag{3.10}
$$

At this point, we should notice that Gauss Markov model depicted by equation (3.2) assumes a linear relationship between the observations y and the unknown parameters ξ. The collinearity equation (3.1), however, shows highly non-linear relationship between the unknown parameters and the observations. In general, the non-linearity is eliminated by performing the linearization provided with initial values for the unknown parameters. In this case, we need to iterate the equation untill the estimates converge. The non-linear observation model is given as follows:

$$Y = a(\Xi) + e \qquad e \sim N(0, s_o^{\,2} p^{-1}) \tag{3.11}$$

Using Taylor's series expansion with some approximate values for the unknown parameters (Ξ_o):

$$Y = a(\Xi_o) + \left(\frac{\partial a}{\partial \Xi}\right)_o \cdot (\Xi - \Xi_o) + \cdots\cdots + e \tag{3.12}$$

Here, we have the assumption that the difference between the initial approximation and the true values $(\Xi - \Xi_o)$ for the unknown parameters is a small vector. Thus, we can neglect higher order terms in equation (3.12). The equation (3.12) can be rewriten as follows:

$$Y - a(\Xi_o) = \left(\frac{\partial a}{\partial \Xi}\right)_o (\Xi - \Xi_o) \tag{3.13}$$

Comparing equation (3.13) with equation (3.2), we can find the corresponding components as follows;

$$y := Y - a(\Xi_o), \quad A := \left(\frac{\partial a}{\partial \Xi_0}\right), \quad and \quad x := (\Xi - \Xi_o) \tag{3.14}$$

Thus, equation (3.14) is similar to equation (3.2). The final vector of unknowns can be computed as:

$$\hat{\hat{\Xi}} = \Xi_o + \hat{x} \quad and$$
$$\hat{D}\{\hat{\Xi}\} = \hat{D}\{\hat{x}\} = \hat{s}_o^{\,2}(A^T pA)^{-1} \tag{3.15}$$

A special concern is required for the coordinates of the GCPs. That is, the accuracy of the GCPs could be either enough for the application or not. In the former case, we can consider the coordinates of the GCPs as error-free, so that it is not to be adjusted. In the latter case, however, we have to consider the errors in the coordinates of the GCPs, and those are needed to be adjusted. The mathematical model for the latter case is given by:

$$\begin{bmatrix} X_{io} \\ Y_{io} \\ Z_{io} \end{bmatrix} = \begin{bmatrix} X_i \\ Y_i \\ Z_i \end{bmatrix} + \underline{e_i} = \begin{bmatrix} X_i^{\,o} \\ Y_i^o \\ Z_i^{\,o} \end{bmatrix} + \begin{bmatrix} dX_i \\ dY_i \\ dZ_i \end{bmatrix} + \underline{e_i} \qquad \underline{e_i} \sim N(0, s_o^{\,2} p_i^{\,-1})$$
$$\begin{bmatrix} X_{io} - X_i^{\,o} \\ Y_{io} - Y_i^o \\ Z_{io} - Z_i^{\,o} \end{bmatrix} = \begin{bmatrix} dX_i \\ dY_i \\ dZ_i \end{bmatrix} + \underline{e_i} \tag{3.16}$$

where

X_{io}, Y_{io}, Z_{io}	are the observed GCPs;
$X_i^{\,o}, Y_i^{\,o}, Z_i^{\,o}$	are the initial values of the observations; and
$\underline{e}_i$	is the noise vector contaminating X_{io}, Y_{io}, Z_{io}.

Note that the left-hand side of equation (3.16) is numerically zero for using the observations themselves as intial values. However, the effect of the errors in the coordinates of the GCPs will smear into the adjustment and affect the estimates of unknown parameters. By combining all the observations and unknown parameters in equation (3.1) and (3.16), we can set up the observation equations for the Grand-Adjustment [Schaffrin, 1997]:

$$\begin{bmatrix} y_1 \\ y_2 \end{bmatrix} = \begin{bmatrix} A_1 & A_2 \\ 0 & I \end{bmatrix} \begin{bmatrix} x_1 \\ x_2 \end{bmatrix} + \begin{bmatrix} \underline{e}_{y_1} \\ \underline{e}_{y_2} \end{bmatrix} \tag{3.17}$$

where

y_1 is an observation vector in the image coordinates;

y_2 is an observation vector in the ground coordinates;

x_1 is an unknow vector in the image coordinates;

x_2 is an unknow vector in the ground coordinates; and

A_i are the matrices of the partial derivatives related to the parameters x_1 and x_2, respectively;

I is an identity matrix; and

$\underline{e}_{y_i}, \underline{e}_{y_2}$ are the noises contaminating y_1, y_2 respectively.

Again, comparing the (3.2) and (3.17), the corresponding elements in the observation equations can be found as:

$$y = \begin{bmatrix} y_1 \\ y_2 \end{bmatrix}, \quad A = \begin{bmatrix} A_1 & A_2 \\ 0 & I \end{bmatrix}, \quad and \quad x = \begin{bmatrix} x_1 \\ x_2 \end{bmatrix} \tag{3.18}$$

3.3.4 Differential Rectification Results

Eleven GCPs covering one ARGON frame were selected from a more recent image map, the orthorectified 1997 RADARSAT SAR, in the polar stereographic coordinates. The positional accuracy of the GCPs is approximately 68m (s_d) [Jezek, 1999], and the vertical accuracy of the DEM is approximately 35m [Liu, 1999]. Besides, there is an uncertainty with respect to the measurable error of the GCPs in the image map. It relates to the spatial resolution of the image map. The position of these points were marked in the image plane by manual pixel-pointing with a relative accuracy of 1-2 pixels, using the cursor on a display. Small, sharp bedrock features exposed along the ground lines were selected with a consideration of its distribution because accurate, well-distributed GCPs are essential for an accurate rectification. Figure 3.4 shows an ARGON image orthorectified by using the differential rectification technique. This image was georeferenced to the 1997 RADARSAT SAR image map that was previously orthorectified with a 100-m spatial resolution in polar stereographic coordinates. The ARGON image was also resampled with a 100-m spatial resolution in polar stereographic coordinates. Using all eleven GCPs in the adjustment resulted in the following RMS residual errors from equation (3.10):

$$RMS_{xy} = \sqrt{\hat{s}_o^{\,2}\, diag((A^T PA)^{-1})} \tag{3.19}$$

$$s_x = 100.72m$$
$$s_y = 99.95\ m$$
$$s_d = 141.90m$$

where

s_x, s_y are RMS errors of x and y coordinates of the estimates of the GCPs

s_d is the residuals in Euclidean distance.

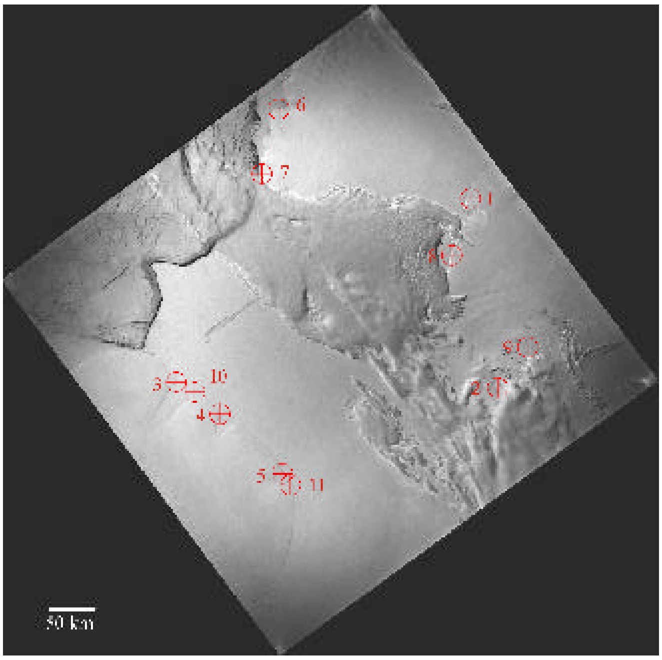

Figure 3.4: The orthorectified ARGON imagery (11/03/63)

In this case, a balance between the observations and the unknowns is as follows:

$$
\begin{aligned}
&\text{number of observations (n)} = (2 + 3) \times 11 = 55 \\
&\text{number of unknowns (m)} = 6 + 3 \times 11 = 39 \\
&\text{Redundancy (n - m)} = 55 - 39 = 14
\end{aligned}
$$

Due to this high redundancy in the measurements, these figures should give a good estimate of the accuracy of the orthorectified image. The distribution of the GCPs and their residual vectors are shown in Figure 3.5.

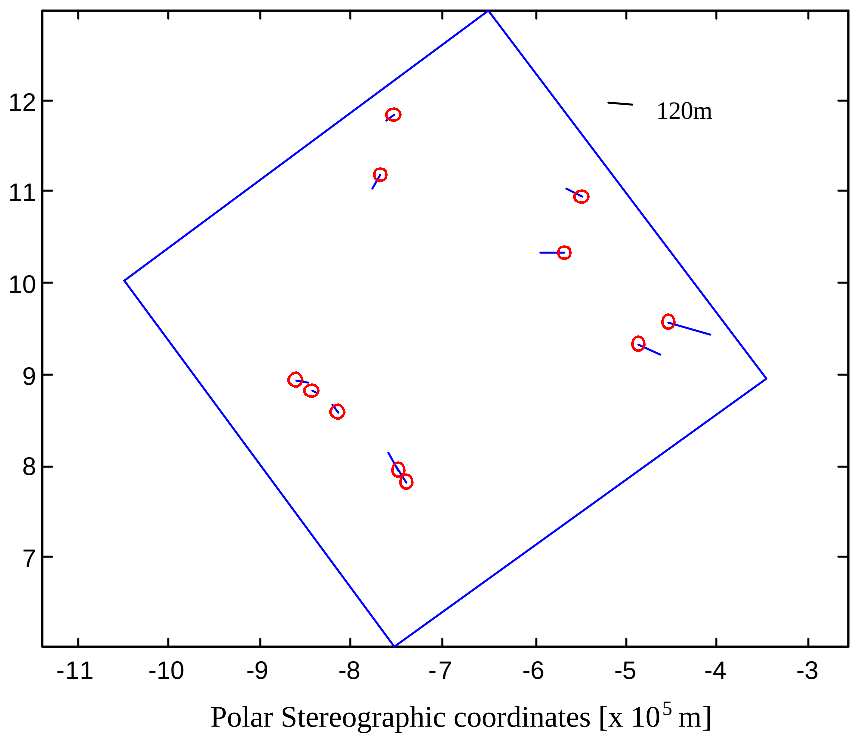

Figure 3.5: Residual error distribution in the orthorectified ARGON image (11/03/63)

The error statistics on the other five ARGON frames, which were used to detect ice front margin of 1963 ARGON image, are listed in the Table 3.1.

Frames	Scene Center(m)		# of GCPs	s_x (m)	s_y (m)	s_d (m)
DS09059A042A079	x	1023159.87	6	97.28	94.337	135.51
	y	1929510.15				
DS09059A010A079	x	198547.28	7	100.19	97.34	139.69
	y	2182437.38				
DS09059A041A079	x	693427.24	8	105.79	104.73	148.86
	y	2073877.00				
DS09059A009A079	x	-154168.06	9	108.04	108.58	153.17
	y	2194070.66				
DS09059A072A078	x	1282149.98	9	94.737	93.592	133.17
	y	2017114.70				

Table 3.1: The error statistics on the other five ARGON frames

3.2.5 First Order Polynomial Rectification for CORONA photography

In general, this technique uses a higher order polynomial to relate the orthorectified image and the original image. The order of the polynomial depends on the terrain type and the number of GCPs available. As the metropolitan areas of Columbus Ohio are relatively small, flat terrain surface, a first order polynomial rectification technique (Affine Transformation) was used to correct geometric correction of CORONA photography. This polynomial shifts, rotates and squeezes the original image to fit the GCPs. This technique is frequently used to rectify satellite imagery.

The mathematical model that relates the image coordinates to the ground coordinates is as follows:

$$\begin{bmatrix} x' \\ y' \end{bmatrix} = \begin{bmatrix} a_0 \\ b_0 \end{bmatrix} + \begin{bmatrix} a_1 & a_2 \\ b_1 & b_2 \end{bmatrix} \begin{bmatrix} x \\ y \end{bmatrix} \tag{3.17}$$

where

(x, y)	are positions in the output-rectified image or map;
(x', y')	are corresponding positions in the original input image;
(a_0, y_0)	are translations that shift the origin of the image coordinate system into the ground coordinate system; and
(a_1, a_2, b_1, b_2)	are parameters that compensate for rotation angles, scale factors, and non-orthogonality between the two coordinate system.

Before applying the rectification to the entire image, it is important to determine how well the six coefficients derived from the least-square adjustments of the initial GCPs account for the geometric distortion in the input image. It can be written as follow:

$$\begin{bmatrix} x_i' \\ y_i' \end{bmatrix} = \begin{bmatrix} 1 & x_i & y_i & 0 & 0 & 0 \\ 0 & 0 & 0 & 1 & x_i & y_i \end{bmatrix} \begin{bmatrix} a_0 \\ a_1 \\ a_2 \\ b_0 \\ b_1 \\ b_2 \end{bmatrix} \tag{3.18}$$

The estimate for the six unknown parameters can be derived from equation (3.17). Using these six coordinate transform coefficients that model distortions in the origianl image, it is possible to transfer pixel values from the original distorted image (x', y') to the grid of the orthorectified output image, (x, y).

The CORONA images were co-registered against 1:24,000-scale Digital Line Graph (DLG) maps by locating thirty control points using a first order polynomial rectification technique. The position of the GCPs selected was mainly a road intersection on the reference maps. Finally, the CORONA imagery was resampled with a 3-m spatial resolution in Universal Transverse Mercator (UTM) coordinates. Using all 30 GCPs in the adjustment resulted in the RMS errors of about 15 meters. Figure 3.6 shows how well the orthorectified CORONA image is fit to the reference maps (solid) on a scale 1:24,000.

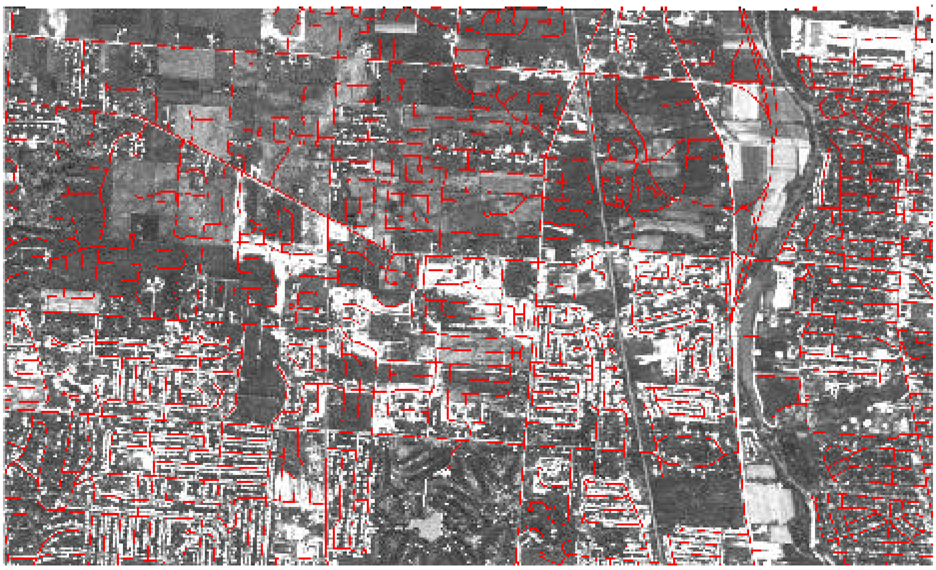

Figure 3.6: Example of image-to-map rectification

3.3 Image Enhancement

Film-grain noise is a factor when processing low contrast images photographed with a very small focal length and aperture cameras such as those carried by ARGON satellites. Film-grain noise is so severe that conventional statistical restoration techniques have little effect. Film-grain noise is produced by a photographic emulsion during the process of recording an image on film.

The films were digitized at 7-µm resolution with a state-of-art scanner. The common feature of film-grain noise is that the power of the noise is related to the brightness of the corrupted pixel. Figure 3.7(a) shows an original image corrupted by film-grain noise. A two-dimensional adaptive noise-removal filtering was applied to the original image. This filtering is useful for an intensity image degraded by constant power additive noise such as film-grain noise because it uses a pixel-wise adaptive Wiener method based on statistics estimated from a local neighborhood of each pixel [Lim, 1990]. Wiener estimates the local mean and variance around each pixel as follows:

$$
\begin{aligned}
m &= \frac{1}{NM} \sum_{n_1, n_2 \in h} a(n_1 - n_2) \\
s^2 &= \frac{1}{NM} \sum_{n_1, n_2 \in h} a^2(n_1, n_2) - m^2
\end{aligned}
\qquad (3.19)
$$

where h is the N-by-M local neighborhood of each pixel in the image, and $a(n_1, n_2)$ is a neighbor pixel around each pixel. Wiener then creates a pixel-wise Wiener filter using these estimates:

$$b(n_{1,}\, n_2) = m + \frac{s^2 - n^2}{s^2}(a(n_{1,}\, n_2) - m) \qquad (3.20)$$

where n^2 is the noise variance, and $b(n_{1,}\, n_2)$ is a filtered pixel. If the noise variance is not given, Wiener uses the average of all the local estimated variances.

The emboss northwest (NW) filter was then applied to transform the image into a relief, making the details appear as ridges and crevices on a flat surface. An ARGON image performed by the adaptive noise-removal filtering and embossing was shown in Figure 3.7(b). A mask applied to emboss the filtered image is as follows:

$$\begin{bmatrix} 2 & 1 & 0 \\ 1 & 1 & -1 \\ 0 & -1 & -2 \end{bmatrix}$$

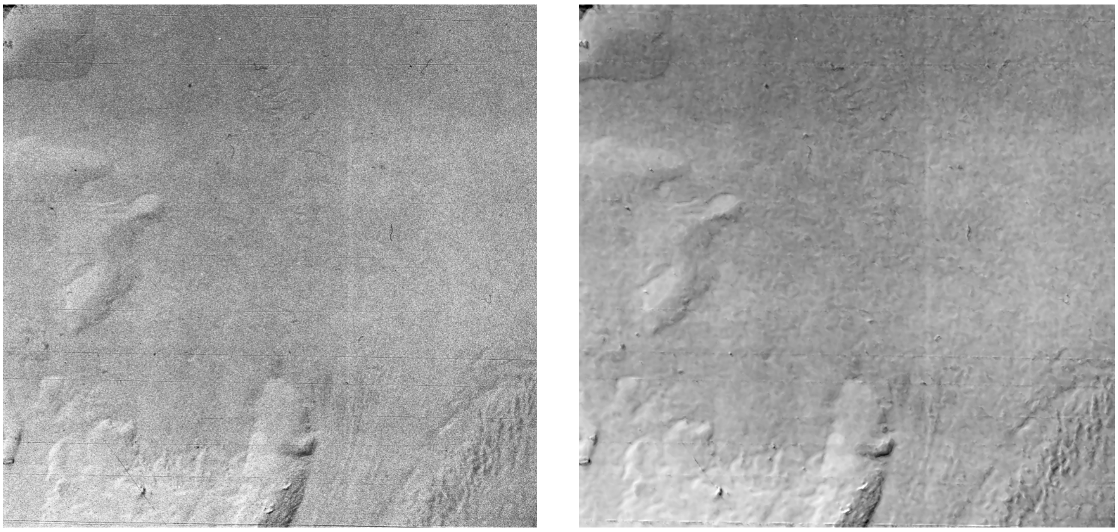

(a) (b)

Figure 3.7: Raw ARGON image (a) and noise filtered, embossed ARGON image (b)

3.4 Image Mosaicking

Digital mosaicking techniques were implemented to join the digital orthorectified images. In this case there were intensity differences that cause artificial edges at the seam between the frames. These intensity differences are due to changes in atmospheric transmittance and in illumination caused by different Sun angles. Seasonal changes of surface reflectance also contribute to the artificial edges in mosaics. Both image frames were acquired ARGON on October 29, 1963. This means that those seams would be mainly caused by the changes in atmospheric transmittance and in illumination angles. Figure 3.8, a mosaic of two rectified, noise-reduced DISP frames from different orbits, shows pronounced artificial edges along the seams.

To eliminate the seams, the radiometric balancing and blending operations were applied to this image. The first radiometric balancing consisted of adjusting the average gray level of each image to the same value. The second correction was achieved by setting the cut-line by considering those intensity differences in the overlap region and performing a blending operation (feathering) from the cut-line to a constant distance across the cut-line. Figure 3.9 shows a complete mosaic of parts of two DISP frames created by linear brightness adjustment and seam smoothing.

Figure 3.8: A mosaic of two DISP frames of the east Antarctic

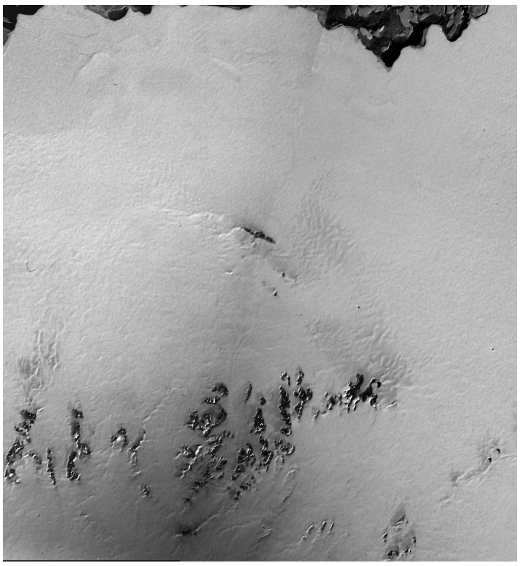

Figure 3.9: A complete mosaic of parts of two DISP frames of the east Antarctic

CHAPTER 4

GLACIOLOGICAL MAPPING OF THE ANTARCTICA ICE SHEET

This application is a demonstration of the usefulness of historic high-resolution satellite images for glaciological studies of Antarctic ice shelf motion and coastline changes.

4.1 Antarctic Ice Sheet

Over the past century, changes in the area and volume of the Antarctic ice sheet have been quantitatively linked to changes in global climate and sea level, which has been slowly rising. Quantitative assessments of how the Antarctic ice sheet dynamics and discharge rates change with changing climate remain elusive. Several questions must be answered to obtain quantitative information suitable for predicting ice sheet behavior. For examples, are glaciers and ice sheets useful indicators of current climate change? How are the interior ice sheet and ice sheet margin changing? What are the velocities and strain rates for different flow regimes? Where are grounding lines located and have they moved? In order to obtain some of the information needed to answer to those questions, ice sheet margins and velocities of Antarctica were measured using 1963 ARGON and 1997 RADARSAT data.

4.2 Mosaic of 1963 ARGON images

Five positive ARGON films that cover a portion of the east Antarctic ice sheet were scanned at 7-microns. Using digital rectification techniques, each digitized image was registered to the previously orthorectified 1997 RADARSAT SAR image map. The RADARSAT image map is provided at 100-m spatial resolution in polar stereographic coordinates. Orthorectified ARGON images were filtered with the adaptive noise-removal filter, and then mosaicked using a radiometric balancing and blending function. The processed ARGON mosaic is shown Figure 4.1. This mosaic spans about 2000-km of coastline from the Fimbul Ice Shelf (4°W and 69°S) to Lützow-Holm Bay (40°E and 72°S). This stretch of coastline is characterized by several ice shelves interrupted by numerous, small ice rises.

Please refer to the separated figure file (Figure 4.1)

Ice shelves form where ice sheets extend outward to the ocean. Ice tongues form where fast moving streams of ice are extruded onto the ocean between lateral barriers, such as ice rises. Figure 4.2 (a) shows that the ARGON data of the Fimbul Ice Shelf reveal extensively crevassed zones caused by the northerly extension of the Jutulglacier into the ice shelf. This also includes Trolltunga, a roughly 90-km long ice tongue, at longitude 1° W. Figure 4.2 (b) shows that a 16-km wide and 7-km long part of the 1963 ice tongue disappeared by 1997. Calving from the snout of ice tongues is a routine occurrence caused by ocean waves flexing the extended tongue.

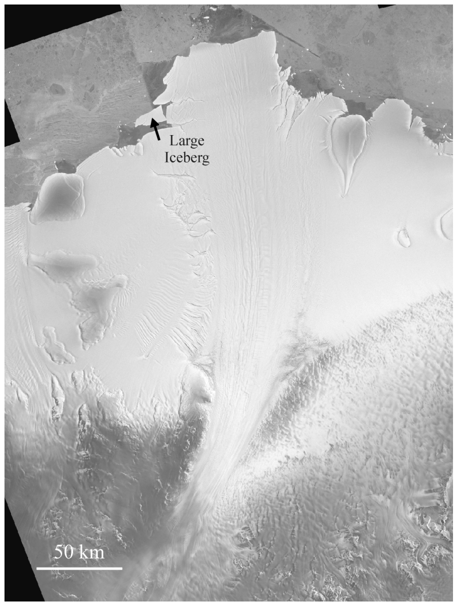

(a) ARGON (October, 1963)　　(b) RADARSAT (September, 1997)

Figure 4.2: Fimbul Ice Shelf

Sea ice covers much of the ocean during the austral winter. In winter the sea around the Antarctic freezes, but ocean swells and wind breaks sea ice into large pieces termed pack ice that move under the influence of wind and currents. However, there are areas where sea ice is trapped within coastal embayments and remains in place for several seasons. This is named fast ice. The optical properties of fast ice make it difficult to distinguish the boundaries between ice sheet and fast ice. Figure 4.3 shows Lützow-Holm Bay as captured by ARGON on October 30, 1963. The coastal area was almost filled with fast ice. The solid line is a coastline manually delineated from 1963 orthorectified ARGON image.

.

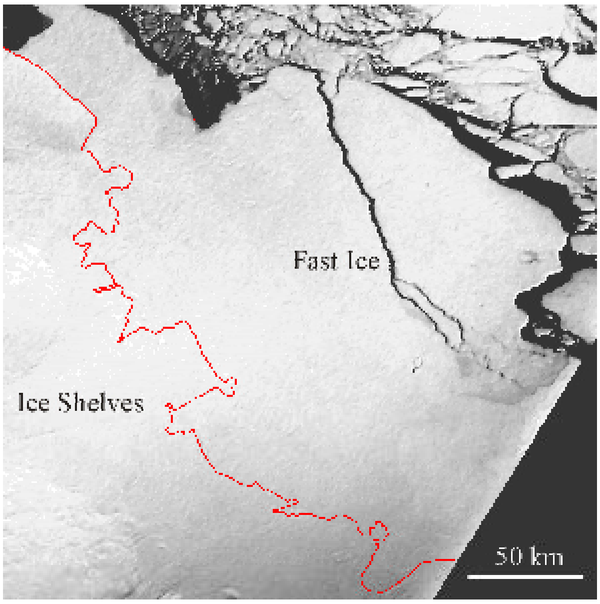

Figure 4.3: Lützow-Holm Bay filled with the huge fast ice (10/30/63)

4.3 Coastline Changes in East Antarctica

Figure 4.4 shows the RADARSAT SAR mosaic corresponding to the same portion of the ARGON mosaic (Figure 4.1). These data were obtained by the Canadian RADARSAT-1, between September 19 and October 14, 1997. RADARSAT–1 is equipped with a C-band SAR capable of acquiring high-resolution (25-m) images of Earth's surface day or night and under all weather conditions. The RADARSAT mosaic was produced by the RADARSAT Antarctic Mapping Project (RAMP) which is a collaboration between the U.S. National Aeronautics and Space Administration and the Canadian Space Agency [Jezek, 1999].

The ice sheet margins on both mosaics were manually delineated. Intermediate images such as late 1980 LANDSAT and mid 1980 AVHRR data were used to better distinguish between fast ice and glacier ice. The coastlines obtained from the 1963 ARGON imagery were compared with those identified in the 1997 RADARSAT SAR imagery. Figure 4.4 shows the coastline changes in the east Antarctic ice sheet between 1963 and 1997. Figure 4.5 shows a relationship between the ice margin change and latitude and their correlation. The results illustrate that the seaward margin of the ice sheet advances and retreats in a complex fashion. Between 0 and 15°E longitude, the ice margin retreated in general. The magnitude of retreat is well correlated with latitude. Between 15 and 35°E longitude, ice margin changes are largely uncorrelated with latitude. The absence of a uniform trend in ice margin advance/retreat with latitude suggests that the ice margin position is controlled by local rather than global processes.

Please refer to the separated figure file (Figure 4.4)

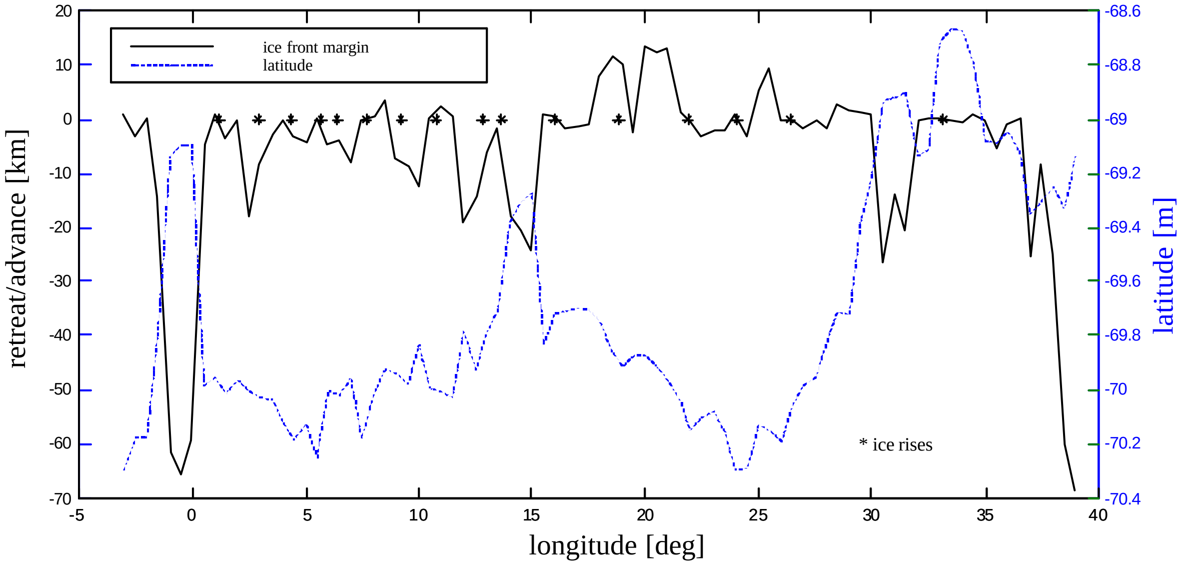

Figure 4.5: Retreat/advance of the east Antarctic ice sheet between 1963 and 1997

4.4 Ice Sheet Velocity

Ice sheets spread and thin at rates controlled by the interaction between forces acting on the surfaces of the glacier and the constitutive relationship between velocity gradients and stress [Jezek, 1999]. It is thus one of the most fundamental parameters in the study of ice dynamics. A rapid and easy way to obtain the velocities and the strain rates of ice sheets in Antarctica involves the use of time series satellite images [Lucchitta and Ferguson, 1986].

Figure 4.6 shows examples of the orthorectified ARGON (left) and RADARSAT SAR (right) image over the Filchner Ice Shelf in Antarctica. Each show distinctive flow and crevasse features in the ice shelf downstream of its grounding zone. Comparison of both images shows a dramatic retreat of the ice sheet margin. In the austral winter of 1986, about 70-km of the front edge of the Filchner Ice Shelf broke off into the sea.

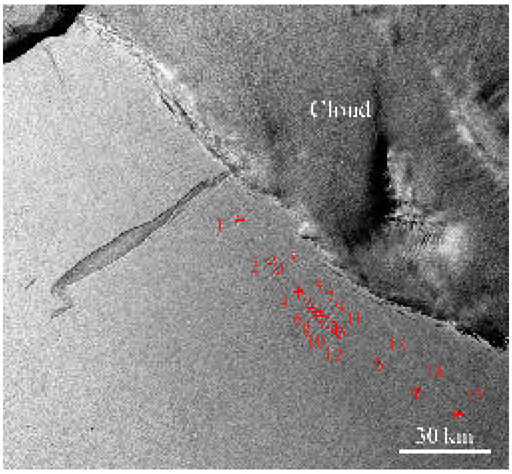

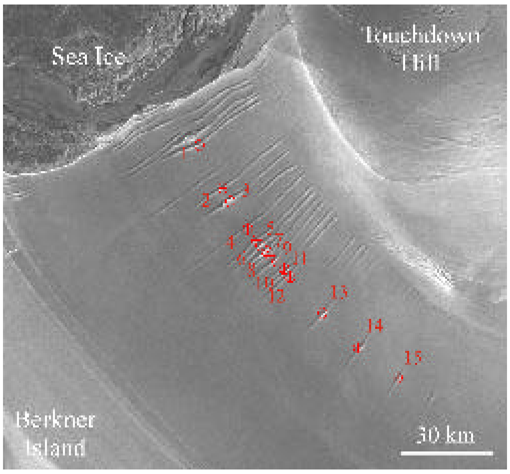

(a) November, 1963 ARGON (b) September, 1997 RADARSAT SAR

Figure 4.6: Ice crevasses on the Filchner Ice Shelf

Fifteen points on ice crevasses were measured on each image map to compute velocities of the Filchner Ice Shelf. Individual, crevasses on both images were identified by simple visual inspection. Repeated measurements resulted in average displacements of the crevasses identified. The computed velocities were compared with more accurate, recent velocity data, which were obtained from SAR interferometric technique [Gary and others, 1998]. ARGON-INSAR velocities on the Filchner Ice Shelf are shown in Table 4.1.

Points	argon_x	argon_y	argon_vel	Insar_x	Insar_y	Insar_vel
1	-697667	904019	667.8	-697165	903437	664.1
2	-711063	911713	692.6	-711909	912706	702.4
3	-723864	920418	723.6	-725203	919713	739.1
4	-736775	930423	755.6	-737776	930740	767.7
5	-737826	931570	756.0	-737776	930740	767.7
6	-738719	932874	754.3	-739528	932802	770.4
7	-741459	934817	765.3	-741177	935069	772.8
8	-743402	936656	762.5	-742855	937145	780.8
9	-744066	938107	785.3	-744532	939311	787.9
10	-745678	939910	781.8	-744532	939311	787.9
11	-746974	941101	790.8	-746348	941477	789.7
12	-750669	944516	799.2	-752217	943782	807.6
13	-757569	951627	829.5	-757317	950210	825.0
14	-759881	955427	832.4	-760740	954541	836.7
15	-769181	968037	846.9	-768495	969422	869.9
Average			769.6			777.9

[m and m/year]

Table 4.1: ARGON and INSAR velocities on the Filchner Ice Shelf.

Each time interval (34 years and 24 days) between the two epochs was standardized for a time difference of one year. The final error in the flow velocities is about $\sqrt{s_{ARGON}^{2} + 2 \times s_{picking}^{2}} \cong 198\,\mathrm{m}$, where s_{ARGON}, the accuracy of orthorectified ARGON image map, is about 140m and $s_{picking}$, the error in picking the crevasses on both orthorectified image maps, about 100m (1 pixel). These span a time interval of 34 years, so that the uncertainty in derived velocity is about 198/34 = 5.8m/year. Comparison of velocities and flow directions of DISP and INSAR are shown in Figure 4.7(a). The sets of each point and average value are comparable each other and show the expected decrease in velocity with distance from the calving front. Error bars of 5.8 m/year are included on the two velocity curves and indicate that at distance up to 80km from the ice margin the velocities are not statistically different. There is a weak suggestion of measurable difference from 80 to 120km. Two velocity data were also mapped in the polar stereographic coordinates (Figure 4.7 (b)). Note that the DISP-RADARSAT velocities are based on displacements that span a time interval during which large pieces of the ice shelf front broke free. The favorable comparison between those average velocities and the 1997 instantaneous velocities suggests that the large calving event did not effect ice shelf dynamics.

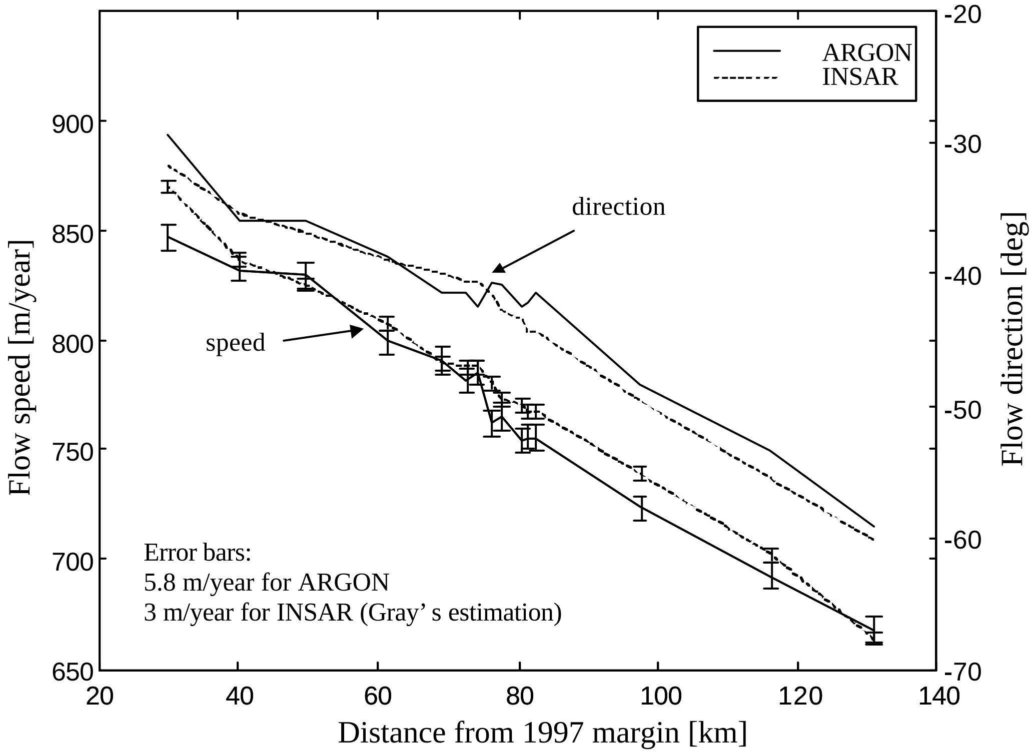

Figure 4.7(a): Comparison of velocities between 1963 DISP and 1997 INSAR

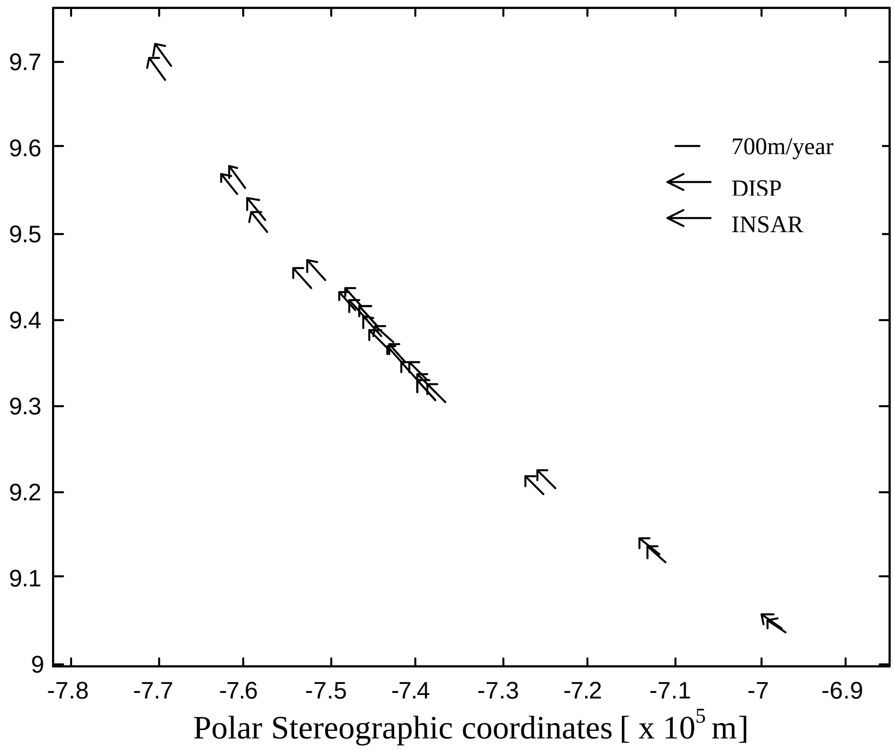

Figure 4.7(b): Comparison of flow directions between 1963 DISP and 1997 INSAR

CHAPTER 5

URBAN MAPPING OF COLUMBUS OHIO, 1965

5.1 Introduction

Growing urban areas modify patterns of local Landuse/Landcover. Land use changes associated with an urban area can be extensive, but the evolution of land usage from rural to urban applications and the resulting impact on the environment and quality of life can be gradual. One way to understand and document land use change and urbanization is to establish benchmark maps. These maps can be compiled from traditional ground surveying and assessment techniques, aerial photography, and more recently, satellite imagery. Satellite imagery is particularly valuable because of accessibility to any part of the world, large spatial coverage for placing changes in a regional context, and increasing resolution for better interpretation. High quality satellite imagery from the Landsat program has been available since 1972. Landsat carried the multi-spectral scanner (MSS) which viewed the earth in 5 spectral bands from the optical to infrared at resolutions from 80m to 240m. Similar instruments followed MSS with current data from the SPOT satellite available at 10m resolution over frames 60 km x 60 km in size [Jensen, 1996].

Until recently, urban researchers were limited to airborne data as a source for high-resolution broad-scale coverage for the era preceding Landsat. Now more extensive coverage at higher resolution has come available through declassification of early satellite reconnaissance photography [MacDonald, 1995]. With these data, we can examine the detailed stages of city development from the 1960s to the present.

In this application, we combined early historical satellite data with more recent land use coverage maps and more recent satellite images. The land use map for this study is the United States Geological Survey Landuse/Landcover map. A Landsat TM image acquired in 1994 is also used. We combined raster data and vector data to monitor changes of the city of Columbus, Ohio over last 30 years.

5.2 Approach

The 1965 reconnaissance satellite imagery consists of 3m resolution filmstrips. Their nominal ground coverage is 17-km x 230-km [Selander, 1995]. Consequently the city of Columbus and its environs are covered with only two image strips. These data were collected with a panoramic camera, so distortion near the two ends of the photograph is large. In our case, our study area lies in the middle of strip and accordingly the geometric distortion is minimal. We extracted the central portion of the strip that covers the city of Columbus and its vicinity. Each selected portion of the strip approximately covers 17-km x 33-km.

The filmstrips were digitized at 7-micron resolution. This is commensurate with the 3-m spatial resolution of the original product. Each digitized image was co-registered against 1:24,000-scale Digital Line Graph maps by locating 30 control points circumscribing the study area. We applied a two-dimensional polynomial linear warping function to the co-registered image to match it to the Digital Line Graph maps. The mean residual of this fit at the control points was 15 m (5 pixels). The two rectified image strips were first mosaicked and radiometrically balanced using a blending function to remove the seamline between the two strips. Urban boundaries were manually delineated (figure 5.1). The first step was to manually assign urban signatures by comparing the 1965 data with attribute files associated with the Landuse/Landcover maps in the city core. A similar approach was used to identify rural type-areas. Then these signatures were manually applied to the rest of the image. In addition, photo-interpretation of features like commercial and industrial building blocks, transportation networks, streams and family home blocks were done. Small rural-type areas (such as the OSU Research Farms) contained within urbanized areas were ignored during boundary mapping.

A Geographic Information System was used to compile and integrate the time series data. Input data sources were comprised of the processed historical high-resolution photographic records, US Geological Survey Landuse/Landcover maps, and Landsat imagery. Urban or built-up land classes of the US Geological Survey Landuse/Landcover maps includes seven sub-categories: residential, commercial and services, industrial, transportation, industrial and commercial complexes, mixed urban or built-up land, and other urban or built-up land [Anderson et al., 1976]. All of these classifications were selected to define urban boundaries. Because they correspond to structures identifiable in the satellite imagery, we believe we have a consistent comparison between the three data sets.

5.3 Results

The processed digital image (figure 5.1) is an intriguing snapshot of the city and its surroundings. It has many important attributes for urban mapping. The filmstrips are extensive enough so that only a few have to be mosaicked to provide contextual information about the city, suburbs and rural environments. The high-resolution data enable easy discrimination between urban and rural areas. Streams, rivers and reservoirs are readily identified. Roads, streets, and highways under construction (e.g. I-270) are evident, as are large buildings, parks, sports facilities, and commercial establishments. Single family homes are not resolvable in the image though some sense of the density of homes can be gained from the texture in the images.

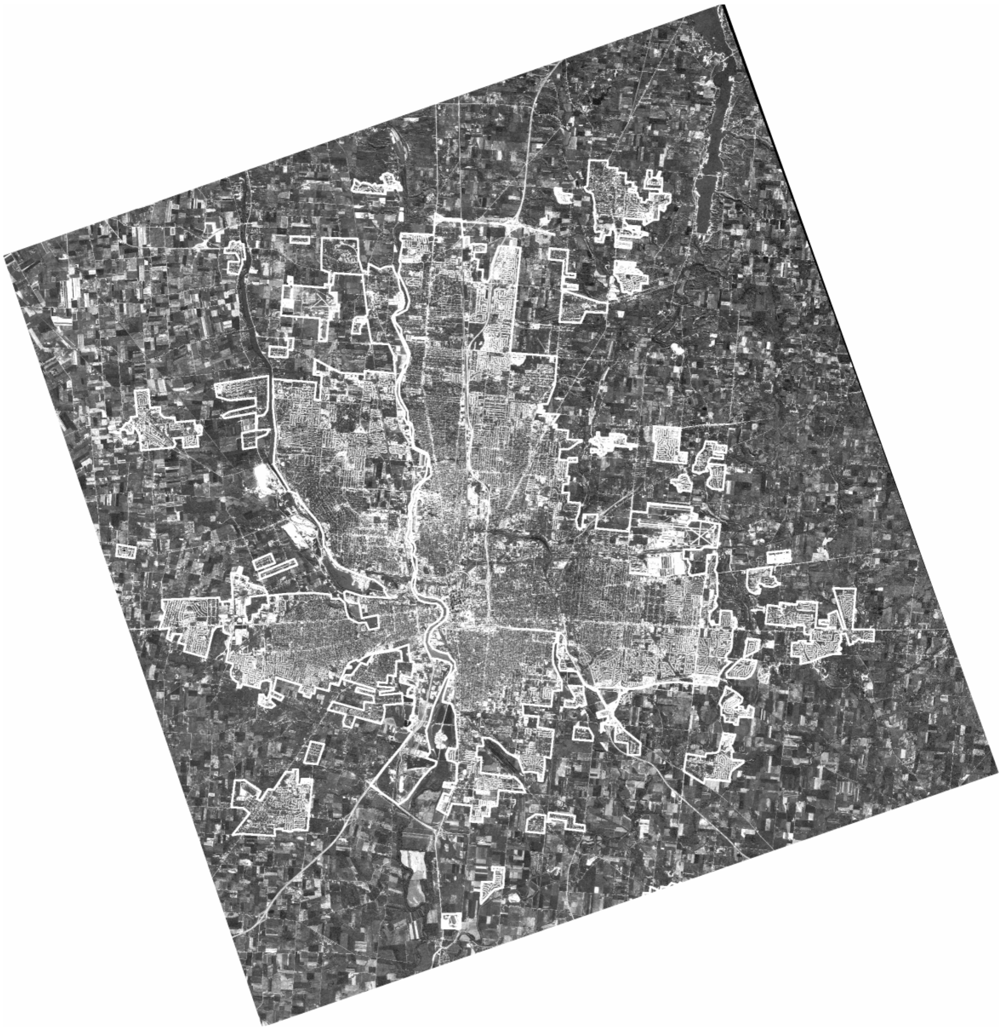

Figure 5.1: Urban boundaries (white) derived from1965 reconnaissance satellite image of metropolitan Columbus

Figure 5.2 illustrates an area around The Ohio State University. The images contrast both high-resolution 1965 data with multispectral 1994 data. At this scale we can clearly see the football stadium and "oval" of the university. The digital image is a remarkable depiction of the city as it was over 34 years ago.

Some areas in the digital image are difficult to classify. For example, figure 5.3 shows an area just west of the Scioto River. The light-colored areas in the 1965 satellite photograph suggest something related to urban development. 1976 Landuse/Landcover maps, however, classifies these areas as non-urban land use type. We conducted fieldwork and found that most of the area is used as a quarry and contains excavation equipment. We observed some new home construction on the north flank of the area.

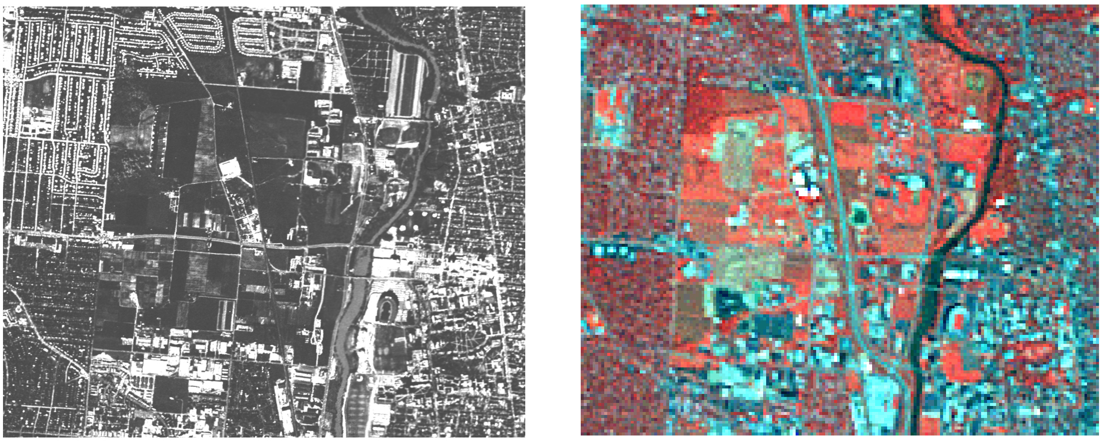

1965 CORONA image (3m) 1994 LANDSAT TM image (25m)

Figure 5.2: OSU and vicinity

Figure 5.3: Quarry along the Scioto River

The 1994 Landsat TM image shown in figure 5.4 is a composite of band 1, 2, 3 and 4. The image pixel size is 25 meters, which represents a slight over sampling of the nominal 30 m Landsat TM pixel. A manual approach similar to the one used for the 1965 image was used to map the urban boundary shown in figure 5.4. While the identification of structural units was more difficult because of the poorer spatial resolution, multi-spectral data overcame this limitation. The trade-offs between resolution and spectral coverage are further illustrated in figure 5.2. The figure shows the region near the Ohio State University and the university farms. Urban structures are easily identifiable in the 1965 image enabling land-use separation. Urban structures are more difficult to identify in the 1994 image but land-use patterns are made evident by their spectral signature.

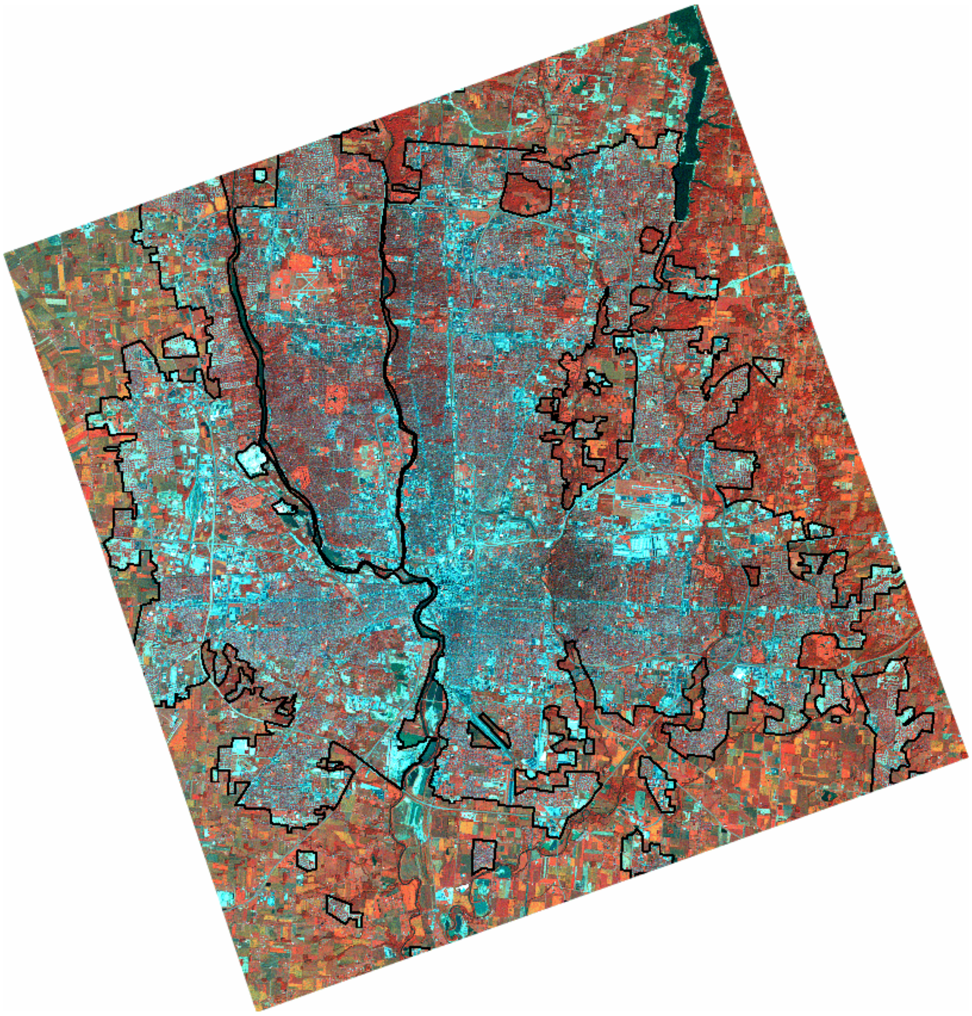

Figure 5.4: Urban boundaries (black) derived from a 1994 Landsat TM image of Columbus, Ohio

Urban change detection maps provide a visualization of the land use cover changes associated with urbanization since 1965. The comparison of the historical high-resolution digital image and the current land use maps illustrates that the urban area of Columbus has expanded largely to the North and East (figure 5.5). Much of the development between 1965 and 1976 is associated with route 40, I-70 and I-71 that are the major east/west and north/south arterial road networks through the city. By 1994, the pattern is more homogeneous probably as a result of the construction of the 1-270 outer belt.

The areal extent of urban development was measured from each data set. The areas were normalized by the area measured in 1994. The results are shown in figure 5.6 Also shown is total population [Taft and Johnson, 1997]. We found that the increase in population is roughly proportional to the increase in urban land use.

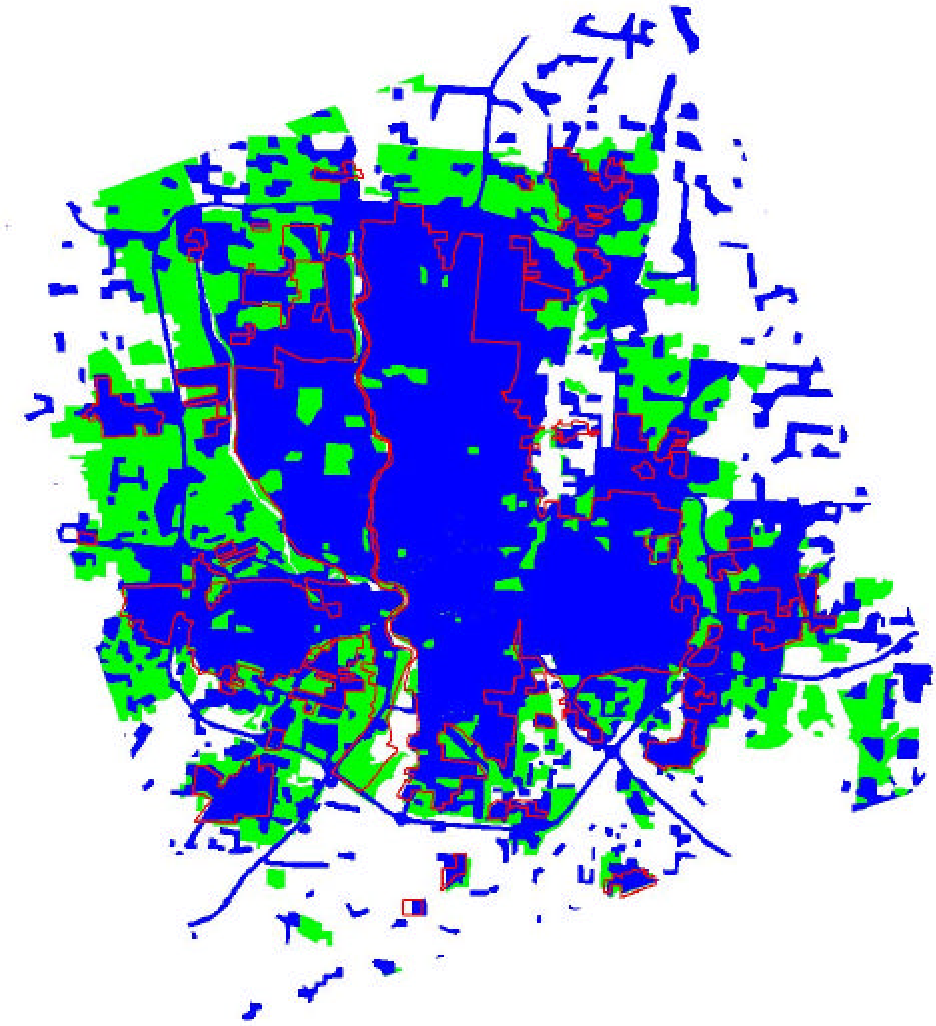

Boundary	Area (Km^2)	Population
1965 (line)	332.512	758,100 (estimated)
1976 (black area)	555.601	851,190 (estimated)
1994 (gray area)	688.647	1,005,164

Figure 5.5: Urban boundary change map

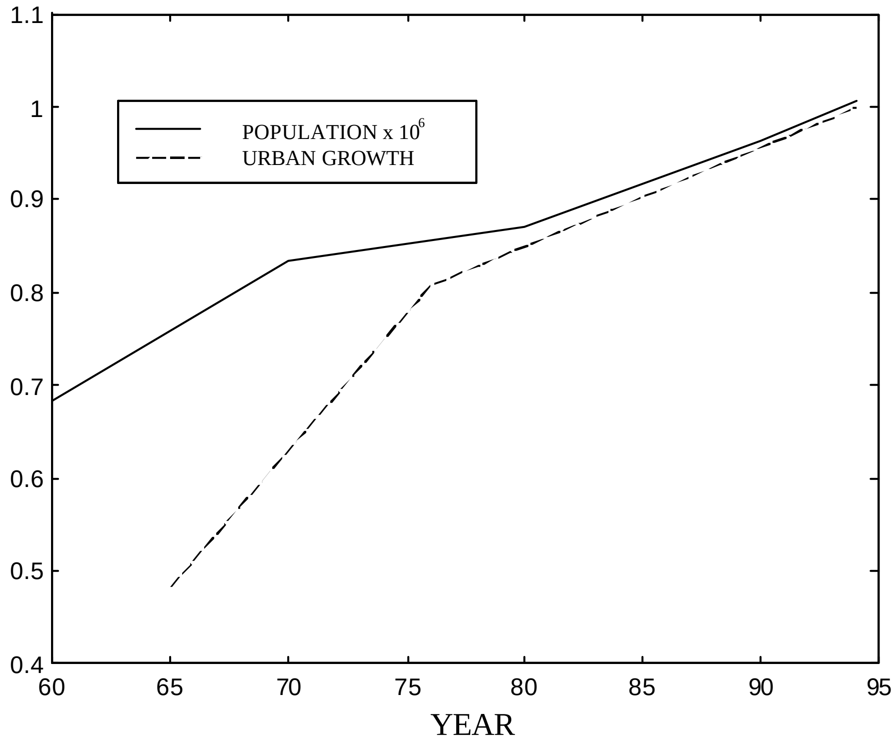

Figure 5.6: Comparison of the change in urbanized area and urban population

5.4 Discussion

Historical satellite data were found to be suitable for establishing a benchmark for land use patterns in and around Columbus, Ohio for 1965. Comparison of these data with later land use maps shows that the urban area in and around Columbus approximately doubled since 1965. The visualization of urban expansion through the time series data contributes to the research and technology base needed to understand land use change and urbanization. The high resolution of the data suggests that additional studies of the growth of transportation networks are also possible.

CHAPTER 6

CONCLUSION

Sophisticated photogrammetric and mapping techniques were employed to derive more accurate positional information about features on Earth surface from declassified historic satellite data. A more rigorous analysis for environmental changes resulted in new scientific applications from precisely orthorectified image maps.

This paper shows the usefulness of declassified historical satellite imagery for glaciological studies of ice shelf motion and ice sheet margin changes in the Antarctic Ice Sheet.

Comparison of ice sheet margin changes between 1963 ARGON and 1997 RADARSAT shows that the seaward margin of ice sheets advances and retreats in a complex fashion. The absence of a uniform trend in ice margin advance/retreat with latitude suggests that the ice margin position is controlled by local rather than global processes. The favorable comparison between the 1963 ARGON velocities and the 1997 RADARSAT instantaneous velocities suggests that the large calving event did not effect ice shelf dynamics.

This paper also shows how historic high-resolution satellite imagery can be used to study patterns of urban development and growth.

Comparison of 1965 CORONA image map with later land use maps shows that the urban area in and around Columbus approximately doubled since 1965. We found that the increase in population is roughly proportional to the increase in urban land use and that residential units occupied most of the extended areas.

BIBLIOGRAPHY

Afek, Y. and A. Brand, 1998, Mosaicking of orthorectified aerial images, Photogrammetric Engineering and Remote Sensing, 64: 115-125.

Anderson, J.R., E.E. Hardy, J.T. Roach, and R.E. Witmer, 1976, "A Land Use and Land Cover Classification System for Use with Remote Sensor Data", US Geological Survey Professional Paper 964, Washington, DC.

Bindschadler, R. and W. Seider, 1998, Declassified intelligence satellite photography (DISP) coverage of Antarctica, NASA/TM-1998.

Bindschadler,. R. A. and T. A Scambos, 1991, Satellite-image-derived velocity field of an Antarctic ice stream, Science, 252: 242-246.

Erdas Field Guide version 8.1 (3rd ed.), ERDAS, Inc.1994.

Ferrigno, J. G., B. K. Lucchitta, K. F. Mullins, A. L. Allison, R. J. Allen, and W. G. Gould, 1993, Velocity measurements and changes in position of Thwaites Glacier/iceberg tongue from aerial photography, Landsat images and NOAA AVHRR data, 17: 239-244.

Fonseca, L.M.G. and B.S. Manjunath, 1996, Registration techniques for multisensor remotely sensed imagery, Photogrammetric Engineering and Remote Sensing, Vol. 62, No. 9, pp. 1049-1056

Gray, A.L., K.E. Matter, and P.W. Vachon, 1998, InSAR results from the RADARSAT Antarctic Mapping Mission Data: Estimation of glacier motion using a simple registration procedure, BPRC Technical Report 98-02, pp10-12.

Habib, Ayman, 1999, GS 624 for winter quarter, The Ohio Sate University.

Hood, J., L., Ladner and R. Champion, 1989, Image processing techniques for digital orthophotoquad production, Photogrammetric Engineering and Remote Sensing, 55: 1323-1329.

Hummer-Miller, S., 1989, A digital mosaicking algorithm allowing for an irregular join "Line", Photogrammetric Engineering and Remote Sensing, 55: 43-47.

Jensen, J. R., Introductory digital image processing: A remote sensing perspective (2nd ed.): Prentice Hall, 1996.

Jezek, Kenneth C., Katy Noltimier, Hong Gyoo Sohn, Hong Xing Liu, Biyan Li, Francois Baumgartner, Kee-Tae Kim, 1999, RADARSAT: The Antarctic Mapping Project, 1998-99 Progress Report.

Leachtenauer, J, K. Daniel, and T. Vogl, 1998, Digitizing satellite imagery: Quality and cost considerations, Photogrammetric Engineering and Remote Sensing, 64: 29-34.
Li, R, 1998, Potential of high-resolution satellite imagery for national mapping products, Photogrammetric Engineering and Remote Sensing, 64: 1165-1169.

Light, D. L., 1993, The national aerial photography program as a geographic information system resource, Photogrammetric Engineering and Remote Sensing, 59: 61-65.

Lillesand, Thomas M. and Kiefer, Ralph W., Remote Sensing and Image Interpretation (3rd ed.): John Wiley & Sons, Inc., 1994.

Lucchitta, B. K. and H. M. Ferguson, 1986, Antarctica: Measuring glacier velocity from satellite images, Science, 28: 1105-1108.

Macdonald, R.A., 1995, "Corona: Success for space reconnaissance, A look into the cold war and a revolution in intelligence", Photogrammetric Engineering & Remote Sensing, Vol. 61. No. 6, pp. 689-720.

NASA, 1995, Ice sheets and glaciers, http://southport.jpl.nasa.gov/nrc/chapter5.html#RTFToC50, NASA, Last access on August 1998.

NASA, Polar ice, http://eospso.gsfc.nasa.gov/NASA_FACTS/polar_ice/ice.html, Last access on January 1999.

Paterson, W. S. B., The physics of glaciers (3rd ed.), Elsevier Science Ltd., 1994.

Rangayyan, R. M., M. Ciuc, and F. Faghih, 1997, Adaptive-neighborhood filtering of images corrupted by signal-dependent noise, 37: 4477-4487.

Scambos, T. A. and R. A. Bindschadler, 1993, Complex ice stream flow revealed by sequential satellite imagery, 17: 177-182.

Scambos, T. A., K. A. Echelmeyer, M. A. Fahnestock, and R. A. Bindschadler, 1994, Development of enhanced ice flow at the southern margin of Ice Stream D, Antarctica, 20: 313-317.

Scambos, T. A., M. J. Dutkiewicz, J. C. Wilson, and R. A. Bindschadler, 1992, Application of image cross-correlation to the measurement of glacier velocity using satellite image data, Remote Sens. Environ., 42: 177-186.

Schaffrin, B.A., 1997, GS 650 for autumn quarter, The Ohio State University.

Selander, J. M., 1995, "Image Coverage Models for Declassified CORONA, ARGON, and LANYARD Satellite Photography – A Technical Explanation".

Swithinbank, C, 1988, Satellite image atlas of glaciers of the world: Antarctica, USGS, professional paper 1368-B.
Taft, B. and C.L. Johnson, 1997, Ohio County Profiles, prepared by the Office of Strategic Research, Ohio Department of Development, Columbus, OH.

US Central Intelligence Agency, 1995, "President Orders Declassification of Historic Satellite Imagery Citing Value of Photography to Environmental Science", Press Release of CIA Headquarters, Langley, VA.

Vaughan, D. G. and M. Johas, 1996, Measurements of velocity of filchner-Ronne Ice Shelf, Filchner-Ronne Ice Shelf Programme (FRISP) Report No. 10.

Westin, T., 1990, "Precision Rectification of SPOT Imagery", Photogrammetric Engineering & Remote Sensing, Vol. 56. No. 2, pp. 247-253.

Williams, Jr. R. S. and J. G. Ferrigno, 1999, Estimated present-day area and volume glacier and maximum sea level rise potential, http://geochange.er.usgs.gov/pub/info/facts/atlas/gl_vol.html, USGS, Last access on May 1999.

Williams, Richard S. and Jane G. Ferrigno, 1998, Coastal-change and glaciological maps of Antarctica, USGS Fact Sheet 050-98.

Zwally, H. J., S. N. Stephenson, R. A. Bindschadler, and R. H. Thomas, 1987, Antarctic ice-shelf boundaries and elevations from satellite radar altimetry, Annals of glaciology, 9: 229-235.